Report title: Reduced and Validated Kinetic Mechanisms for Hydrogen-CO-air Combustion in Gas Turbines

Type of Report: Final Scientific/Technical Report

Reporting Period Start Date: February 8, 2006

Reporting Period End Date: February 7, 2010

Principle Investigator: Yiguang Ju and Frederick L. Dryer, Princeton University

Date Report Issued: March 1, 2010

DOE Award Number: DE-FG26-06NT42716

Submitting Organization: Princeton University

Disclaimer

Abstract

Rigorous experimental, theoretical, and numerical investigation of various issues relevant to the development of reduced, validated kinetic mechanisms for synthetic gas combustion in gas turbines was carried out – including the construction of new radiation models for combusting flows, improvement of flame speed measurement techniques, measurements and chemical kinetic analysis of $H_2/CO/CO_2/O_2$/diluent mixtures, revision of the H_2/O_2 kinetic model to improve flame speed prediction capabilities, and development of a multi-time scale algorithm to improve computational efficiency in reacting flow simulations.

Table of Contents

Executive Summary

Rigorous experimental, theoretical, and numerical investigation of various issues relevant to the development of reduced, validated kinetic mechanisms for synthetic gas combustion in gas turbines was carried out – including the construction of new radiation models for combusting flows, improvement of flame speed measurement techniques, measurements and chemical kinetic analysis of $H_2/CO/CO_2/O_2$/diluent mixtures, revision of the H_2/O_2 kinetic model to improve flame speed prediction capabilities, and development of a multi-time scale algorithm to improve computational efficiency in reacting flow simulations.

An accurate spectral dependent radiation model is developed to predict flame speed and flammability of $H_2/CO/CO_2/H_2O$/Air mixtures. The results showed that radiation reabsorption significantly extended the flammability limits. It was also demonstrated that accurate prediction of coal syngas flammability is not possible without appropriate consideration of radiation absorption by CO_2 and H_2O.

Methodologies to improve flame speed measurement were developed by experimental and theoretical investigation of the effect of non-spherical (i.e. cylindrical) bomb geometry on the evolution of outwardly propagating flames and the determination of laminar flame speeds. The cylindrical chamber boundary modifies the propagation rate through the interaction of the wall with the flow induced by thermal expansion across the flame (even with constant pressure), which leads to significant distortion of the flame surface for large flame radii. It was determined that these departures from the unconfined case, especially the resulting non-zero burned gas velocities, can lead to significant errors in flame speeds calculated using the conventional assumptions, especially for large flame sizes.

The methodology to estimate the effect of nonzero burned gas velocities is applied to correct the flame speed for non-zero burned gas speeds, in order to extend the range of flame radii useful for flame speed measurements. Under the proposed scaling, the burned gas speed can be well approximated as a function of only flame radius for a given chamber geometry – i.e. the correction function need only be determined once for an apparatus and then it can be used for any mixture. Results indicate that the flow correction can be used to extract flame speeds for flame radii up to 0.5 times the wall radius with somewhat larger, yet still acceptable uncertainties for the cases studied. Flow-corrected flame speeds in the small cylindrical chamber used here agree well with previously reported flame speeds from large spherical chambers.

Experimental measurements of flame speeds and burning rates, analysis of the key reactions and kinetic pathways, and modeling studies were performed for $H_2/CO/O_2$/diluent flames spanning a wide range of conditions: equivalence ratios from 0.85 to 2.5, flame temperatures from 1500 to 1800K, pressures from 1 to 25 atm, CO fuel fractions from 0 to 0.9, and dilution concentrations of He up to 0.8, Ar up to 0.6, and CO_2 up to 0.4. The experimental data show negative pressure dependence of burning rate at high pressure, low flame temperature conditions for all equivalence ratios and CO fractions as high as 0.5. Dilution with CO_2 was observed to strengthen the pressure and temperature dependence compared to Ar-diluted flames of the same flame temperature. Simulations were performed to extend the experimentally studied conditions to conditions typical of gas turbine combustion in Integrated Gasification Combined Cycle processes, including preheated mixtures and other diluents such as N_2 and H_2O.

Substantial differences are observed between literature model predictions and the experimental data as well as among model predictions themselves – up to a factor of 3 at high pressures. The present findings suggest the need for several rate constant modifications of reactions in the current hydrogen models and raise questions about the sufficiency of the set of

hydrogen reactions in most recent hydrogen models to predict high pressure flame conditions relevant to controlling NO_x emissions in gas turbine combustion.

An updated H_2/O_2 chemical-kinetic model was formulated to address the difficulties observed in modeling the high-pressure flame data. The model incorporates a number of rate constant expressions that are more consistent with elementary reaction studies, particular for the reactions most important for high-pressure flame predictions such as $H+O_2(+M)=HO_2(+M)$, $HO_2+H/O/OH/HO_2$, and $H+OH+M=H_2O+M$. However, substantial fundamental issues and rate constant uncertainties still remain. The updated model reproduces a wide variety of the homogeneous validation targets flame speed validation targets with generally improved agreement against high-pressure flame targets.

Analyses were performed and new algorithms developed in order to improve the computation efficiency of chemical reaction calculations as part of chemically reacting flow simulations. In numerical simulations of combustion process, solution of the chemical kinetics equations is often the most expensive part of the calculation, to such a large extent in some cases that detailed chemistry cannot be effectively implemented in the flow simulation. Several schemes which are widely used in combustion simulation are compared, and a new methodology was developed to construct detailed mechanisms by dynamic multi-time scale method, which in essense calculates the reaction rates of different reactions according to the time scale of their species. Since there are many species which time scales are much larger than the minimum time scale, they can be calculated with larger time steps, much time can be solved. This idea is demonstrated here to improve computational efficiency by an order of magnitude.

1. Experimental and numerical methods

1.1 Experimental apparatus for outwardly propagating flames

Experiments were conducted in a dual-chambered, pressure-release type high-pressure combustion apparatus shown in Fig. 1. Complete details of the experimental apparatus and procedure can be found in Refs. [1-6]. The chamber consists of two concentric cylindrical vessels of inner diameters 10 and 28 cm. The length of the inner chamber is 15.24 cm. Twelve circular holes of 2.2 cm diameter are located in the radial wall of the inner vessel at z-offsets of -4.6, 0, and 4.6 cm and θ-offsets of 45, 135, 225 and 315 degrees to allow for pressure release. These holes can be sealed with O-rings under the compression of iron plates attracted by a series of permanent magnets embedded in the wall. The iron plates provide a seal between chambers for pressure differences between outer and inner chambers greater than 0.3 atm. When the pressure difference vanishes or reverses, the iron plates dislodge, allowing gases to flow from the inner to the outer chamber to maintain a nearly constant pressure. Since the inner vessel volume is 10 times smaller than that of the outer, the total pressure increase after combustion is small, ensuring not only a nearly constant-pressure experiment, but operational safety for experiments conducted at high initial unburned gas pressures. For the present experiments, however, the magnetic plates were either removed entirely, or remained in place (holes sealed) throughout each experiment to avoid transitions in flow field boundary conditions. The two configurations described will hereafter be called "open" chamber and "closed" chamber experiments, respectively. It should be noted that the inner cylindrical wall has cavities leading to the magnetic plates as well as gas inlet and outlet holes. Thus, some aberration in the flame evolution from the perfectly cylindrical case is expected to be present at large flame radii (as the flame structure approaches the side wall holes).

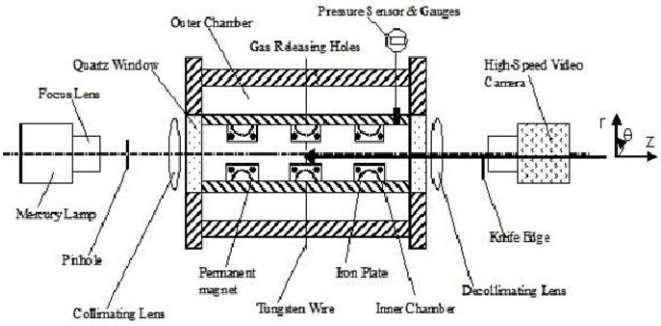

Fig. 1. Experimental apparatus for outwardly propagating flames.

Schlieren photography was utilized for imaging the flame propagation. (Exemplar images are presented in Fig. 2.) Light from a 100 W mercury lamp is focused on a 100 μm pinhole and collimated by a

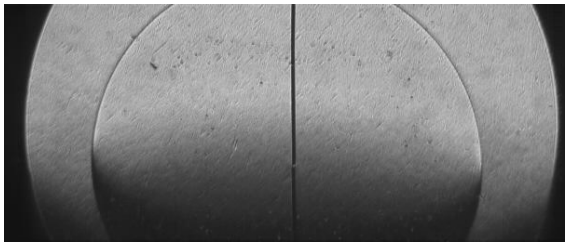

(a) 1 atm

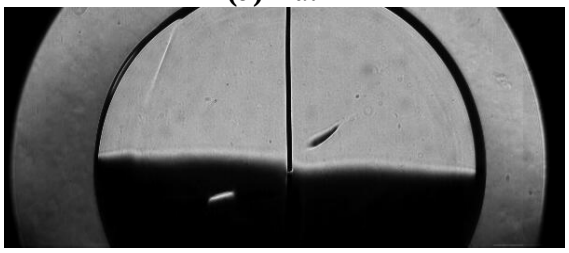

(c) 25 atm

Fig. 2. Schlieren images of propagating flames at $r_f = 2.5$ *cm* for an H_2/O_2/Ar mixture of equivalence ratio 2.5 and flame temperature of ~1600K for various pressures.

spherical lens. The collimated light passes through windows to the inner chamber and is focused on a horizontally installed knife edge. A high-speed digital video camera with 4 μs shutter speed and frame rates of 8,000 to 24,000 fps is used to record images of the propagating flame. The flame front is located from these images and the flame radius along $\theta = 0^o$, r_f, is obtained using an automated detection program for ease of processing and reduction of human bias. The raw r_f data are smoothed and radial propagation speed, $V_{f,r}$, is calculated using local, least-squares 2nd order polynomial fitting methods for data within 3 mm of the radius of interest. Data processed in this manner are consistent with the raw data as well as data processed through a more conventional local-averaging (low-pass) filter.

1.2 Numerical model for outwardly propagating flames in cylindrical confinement

A simple model for flame propagation was used to qualitatively and quantitatively describe the effect of flow field asymmetries on the evolution of an initially spherical flame in the early stages of propagation, where the effect of confinement is nontrivial but weak. In a manner similar to front-tracking methods described in [7, 8], the flame is described by a flamelet model and the flow field is treated as incompressible with a distributed source term for thermal expansion at the flame front and a uniform sink term for compression of the fluid. The flow is further approximated as irrotational (which is reasonable for small r_f, but cannot be ignored for large r_f as discussed below). A weakly stretched flamelet model, i.e. Eq. (16) below, is used with κ, the local instantaneous stretch rate, defined as $d\ln(A_f)/dt$, with A_f being the area of an infinitesimal flame surface element. The boundary conditions for the closed cylindrical chamber used were inviscid walls. The initial condition is a spherical flame of flame radius of $0.1r_w$, with the stretch rate and flame speed of an unconfined flame given by Eqs. (14) and (15) below. The numerical results are smoothed using a locally weighted scatter smoothing (i.e. LOWESS) scheme [9] to remove oscillations introduced by the numerical scheme.

The flamelet model requires input values for s_u^o, L_u, and σ. Where s_u^o, L_u, and σ are chosen to represent experimental mixtures, values for s_u^o and L_u were calculated from the experimental data through a linear regression of Eq. (16) using the flow-corrected flame speed presented in the next section. Expansion factors, σ, were obtained from planar flame calculations [10] using the thermochemical parameters of Li et al. [11].

2. Results and Discussion

2.1 Numerical algorithm for effect of spectral radiation on flame speed

The strong spectral radiation absorption of H_2O, CO, CO_2 and the appearance of large amount of $H_2O/CO/CO_2$ in the syngas raises the following question: what is the role of $H_2O/CO/CO_2$ radiation in flame speed and flammability limit? This concern becomes more serious when the ambient pressure increases.

For combustion gas radiation properties, a number of databases have been compiled based on line-by-line (LBL) [12, 13], and narrow band [14-15] model, and global full-spectrum model [16, 17]. The LBL is accurate at low temperatures, but requires excessive CPU time and is not suitable for high temperature combustion gases because the high temperature vibration-rotation absorption bands are not included. For global models, the weighted-sum-of-grey-gases (WSGG) model [16] and the full-spectrum correlated-k methods [17] were developed. These models have excellent computation efficiency but less accurate than the band models and have difficulties treating non-gray boundaries. The statistical narrow-band (SNB) models [14] are

favored. Recent CO_2 absorption experiment [17] showed that EM2C SNB model has an excellent accuracy up to 1300 K. In the SNB model for non-homogeneous mixtures, the ray tracing method [18] and the Curtis-Godson approximation were widely used [18, 19]. However, the ray tracing method is computationally inefficient, and the Curtis-Godson approximation is accurate only in the optically thick and thin limits.

Lacis et al. [20] developed a new category of the SNB based correlated-k method (SNBCK). By reordering the absorption coefficients in LBL into a monotonic k-distribution in a narrow spectral range, the model can produce exact results at a small computation cost [21]. For inhomogeneous media, it was shown that CK model gives much better results than the standard Curtis-Godson correlation. Furthermore, it allows the implementation of conventional discrete ordinate method (DOM) [22]. However, the inversion of CK model requires numerical iterations and sometimes convergence is not guaranteed. In addition, the SNB-CK model has not been considered in radiation modeling for spherical flames.

In this study, to resolve the convergence difficulty of SNB-CK in multi-component mixtures and to accelerate the computation efficiency, we developed a fitted SNB-CK model and extended it for radiation calculation of spherical flames. Hereafter, we call this model FSNB-CK.

In the SNB model, the gas transmissivity,τ_ν, at wave number ν over a light path L is given as [23]

$$\tau_\nu = \exp\left[-\pi b\left(\sqrt{1+4SL/\pi b}-1\right)/2\right] \tag{1}$$

where $b = 2\bar{\beta}_\nu/\pi$, $S = \bar{k}_\nu Xp$, and $\bar{\beta}_\nu = 2\pi\bar{\gamma}_\nu/\bar{\delta}_\nu$ are the SNB model parameters [14] for CO, CO_2 and H_2O. The bandwidth is 25 cm^{-1} for wave numbers between 150 and 9300 cm^{-1}. By performing an inverse Laplace transformation, the distribution function of the absorption coefficient at each narrow band can be obtained as [20]

$$f(k) = 0.5k^{-3/2}(bS)^{1/2}\exp\left[0.25\pi b\left(2-S/k-k/S\right)\right] \tag{2}$$

and the cumulative function of k-distribution

$$g(k) = \int_0^k f(k')dk' \tag{3}$$

can be given as

$$g(k) = \frac{1}{2}\left[1-\mathrm{erf}\left(\sqrt{\frac{\pi bS}{4k}}-\sqrt{\frac{\pi bk}{4S}}\right)\right]+\frac{1}{2}\left[1-\mathrm{erf}\left(\sqrt{\frac{\pi bS}{4k}}+\sqrt{\frac{\pi bk}{4S}}\right)\right]\exp(\pi b) \tag{4}$$

Using the cumulative distribution function, the average radiation intensity at each narrow band can be calculated using a Gauss type quadrature [21]

$$I_\nu = \sum_{i=1}^{N}\omega_i I_\nu[k_i(g_i)] \tag{5}$$

where N is the number of Gaussian quadrature points, ω_i the weight function, and g_i the Gaussian point. The estimation of $k_i(g_i)$ from Eq. 4 needs iterations and sometimes diverges for multi-component mixtures [20]. In order to resolve this problem, we rewrote Eq. 4 as

$$k_{ii}/S(b)=F_i(b),\ i=1,\ N \tag{6}$$

Here $F_i(b)$ is a fitted function at all Gaussian points for CO, CO_2 and H_2O using the SNB data [14], respectively. Therefore, Eq. (4) is replaced by Eq. (6) using $3\times N$ fitted functions. Since a four-point Gaussian quadrature is accurate enough for Eq. (5), we only need 12 fitting functions. These fittings are straight forward and the maximum error between B=10^{-4} and 10^4 for

k_i/S is less than 0.5%. For b<10^{-4} and b>10^4, the optically thin and thick limits can be applied. The use of Eq. 6 and high accuracy of fitting completely removed the need of iteration for $k_i(g_i)$ from Eq. (4) and thus this technique avoids the problem of divergence.

For radiating gas mixtures, the approximate treatment of overlapping bands from optically thin and thick limits [20-21] was employed

$$S = S_{CO} + S_{CO_2} + S_{H_2O}, \quad S^2 / b = S_{CO}{}^2 / b_{CO} + S_{CO_2}{}^2 / b_{CO_2} + S_{H_2O}{}^2 / b_{H_2O} \tag{7}$$

The contribution from soot radiation at each narrow band can be added to the gas phase radiation. The spectral radiative transfer equation in spherical coordinates at each band in m direction is given as

$$\mu_m \frac{\partial I_{\nu m}}{\partial r} + \frac{2\mu_m I_{\nu m}}{r} + \frac{1}{r}\frac{\partial}{\partial \mu_m}[(1-\mu_m{}^2) I_{\nu m}] = -k_\nu I_{\nu m} - k_\nu I_{b\nu} \tag{8}$$

where μ_m=cos(θ_m), and m is the index from *1* to M of polar angle θ, and I_b the blackbody radiation intensity.

By using the following angular derivative,

$$\frac{\partial}{\partial \mu_m}[(1-\mu_m{}^2) I_{\nu m}] = \frac{\alpha_{m+1/2} I_{m+1/2} - \alpha_{m-1/2} I_{m-1/2}}{\omega_m} \tag{9}$$

$$\alpha_{m+1/2} - \alpha_{m-1/2} = -2\omega_m \mu_m, \ \alpha_{1/2} = \alpha_{M+1/2} = 0$$

and the central difference scheme for spatial and angular discretizations,

$$2I^C_{i+1/2,m} = I_{i,m} + I_{i+1,m} = I^C_{i+1/2,m+1/2} + I^C_{i+1/2,m-1/2} \tag{10}$$

the final discretized radiation transfer equation for μ_m<0 becomes

$$2|\mu_m| \frac{I^C_{\nu,i+1/2,m} - I_{\nu,i+1,m}}{r_{i+1} - r_i} + \frac{(\alpha_{m+1/2} + \alpha_{m-1/2})(I^C_{\nu,i+1/2,m+1/2} - I^C_{\nu,i+1/2,m})}{r_{i+1/2}\omega_m} = k_\nu(-I_{\nu,i+1/2,m} + I_{b\nu,i+1/2}) \tag{11}$$

The boundary conditions at r = 0 and $r = r_2$ are given as

$$I_m = I_{M+1-m} \text{ at } r = 0; \quad I_m = \varepsilon_w I_{bw}(T_w) + (1-\varepsilon_w) \sum_{\mu_m>0} I_m w_m \mu_m / \pi \text{ at } r = R \tag{12}$$

The total volumetric heat source term of radiation is given as

$$\dot{q}_r = \sum_{j=1}^{N-band} \Delta\nu \sum_{n=1}^{N} \omega_n k_n \left(\sum_{m=1}^{M} I_{j,n,m} - 4\pi I_{b\,j} \right) \tag{13}$$

The effects of spectral radiation absorption on the flame speed at normal and elevated pressures were experimentally and numerically investigated using the CO_2 diluted outwardly propagating CH_4-O_2-He flames. Experimentally, the laminar burning velocities of CH_4-O_2-He-CO_2 mixtures at both normal and elevated pressures (up to 5 atm) were measured by using a pressure-release type spherical bomb. The results showed that radiation absorption with CO_2 addition increases the flame speed and extends the flammability limit. In addition, it was also shown that the increase of pressure augments the effect of radiation absorption.

Previous analysis in [24] shows that radiation absorption has less effect as pressure increases because the total chemical heat release increases with the pressure. In order to examine the effect of pressure, the radiation absorption effect and comparison of different radiation model for CH_4+{$0.3O_2$+0.2He+$0.5CO_2$} mixtures at 2 atm is shown in Fig. 2. It is seen that radiation absorption render that optically thing model (OPTM) invalid. In addition, the SNB gray model over-predicts the flam speed and burning limit. The present FSNB-CK model predicts much better flame speeds compared to the experimental data. In addition, by comparing the results with that at one atmosphere, it is seen that the radiation effect becomes much stronger at 2 atm. Different from the previous theory [24], the present result shows that radiation absorption increases with pressure. This is because an infinite optical thickness was assumed in the theory so that all the radiation heat loss from the burned zone will be absorbed by the unburned mixture. In the present experiment, the optical thickness is finite (about 1.0~6.0 estimated from OPTM) so that the increase of pressure enlarges the optical thickness and radiation absorption. Therefore, for syngas combustion with high CO and H_2O concentrations, neither adiabatic nor optically thin radiation model can predict accurate flame speeds for the validation of kinetic model.

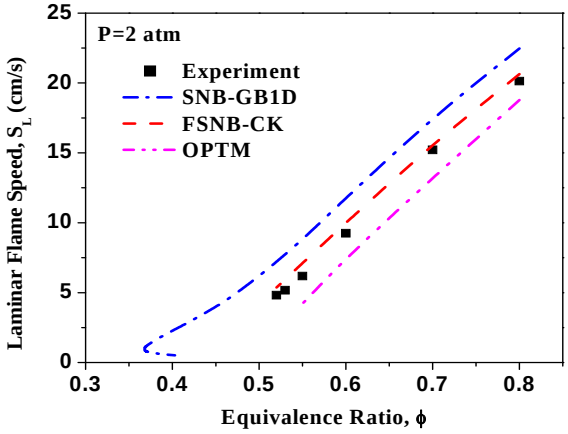

Fig.3. Measured and predicted laminar flame speeds of CH_4-{$0.3O_2$+0.2He+$0.5CO_2$} flames as a function of equivalence ratio at 2 atm.

2.2 Effect of cylindrical confinement on laminar flame speed measurement

The constant-pressure spherical flame method involves capturing Schlieren images of an expanding spherical flame and calculating the instantaneous flame speed and stretch from radius-time data [27, 28]. Most studies employ the relations given by Strehlow and Savage [30] for an unconfined outwardly propagating spherical flame, in which the burned gas is assumed to come to rest after crossing the flame and the flame is taken to be infinitesimally thin:

$$s_{u,unc} = \frac{1}{\sigma}\frac{dR_f}{dt} \tag{14}$$

$$\kappa_{unc} = \frac{2}{R_f}\frac{dR_f}{dt}. \tag{15}$$

Here $s_{u,unc}$ is the uncorrected stretched flame speed, κ_{unc} the uncorrected stretch rate, R_f the spherical flame radius, and dR_f/dt the flame propagation speed, V_f. The thermal expansion factor, σ, is defined as the ratio of unburned to burned gas density. Equations (14) and (15) will henceforth be referred to as the unconfined relations. There are various methods found in the literature for relating stretch rate and stretched flame speeds such that the fundamental mixture parameters, the unstretched laminar burning velocity, s_u^o, and Markstein length, L_u, can be extracted as described in Refs. [27, 31-34]. The present study uses a commonly employed relation, first postulated by Markstein [31]:

$$s_u = s_u^o - L_u \cdot \kappa . \quad (16)$$

Equation (16) was derived from asymptotic theory for weakly stretched flames and has been found to hold for more general conditions. The unstretched laminar burning velocity and the Markstein length can be extracted from experimental data through a linear regression analysis (Eq. 16).

The present study explores the effects of cylindrical-geometry confinement on outwardly propagating flames and the determination of laminar flame speed. The primary focus is on the manifestation of this effect in the flame shape evolution, flame propagation speed, and burned gas speeds along the *r*-axis in chambers having a length greater than their diameter. These factors and conditions encompass all of the research conducted previously in cylindrical chambers [25, 1, 35, 37-39].

Figure 4 presents the experimental data for flame propagation speed history along the *r*-axis of a closed cylindrical chamber for equivalence ratios of 1.0 and 3.0 and the numerical solution of the flamelet model for a cylindrical chamber of the same aspect ratio as the experiment. These results are contrasted with flame speed data obtained in a large spherical chamber ($R_{w,sph} = 30cm = 6r_w$) from [32], simulations for a spherical chamber of the same size ($R_{w,sph} = 30cm = 6r_w$) using direct numerical simulation (in-house code, ASURF-1D, described in detail and validated in [26]), and calculations based on the unconfined flame relations, (14) and (15).

The experimental data and the model solution for the cylindrical chamber are nearly identical to the unconfined model as well as experimental data and A-SURF-1D predictions for the large spherical chamber, during the early stages of propagation ($r_f < 0.3r_w$). For these conditions, the flow field is relatively unaffected by the cylindrical boundary. The radial flame propagation speed initially increases with r_f due to an increase in the unburned flame speed with decreasing stretch and a positive Markstein

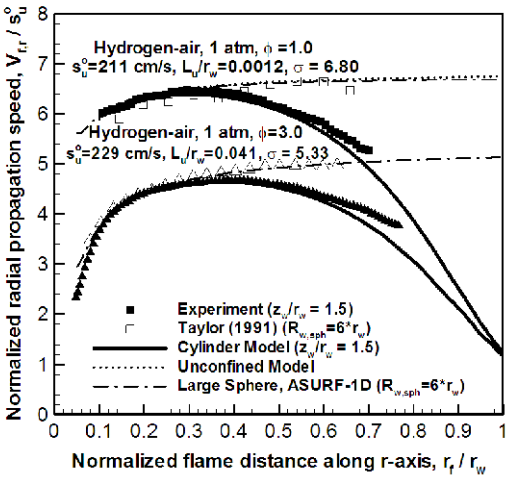

Fig. 4. Normalized flame propagation speed in the radial direction: comparison of experimental traces with model results for flames in a small cylindrical chamber, and experimental and numerical results for flames in a large spherical chamber [32].

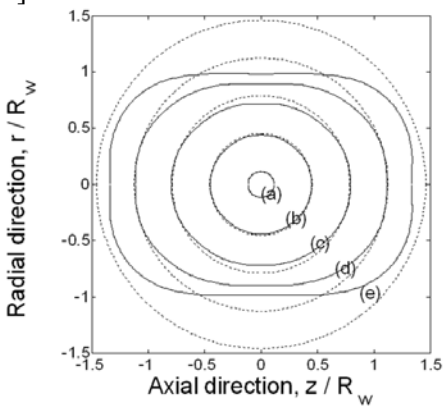

Fig. 5. Comparison of flame surface contours for a flame in a finite-length cylindrical chamber of aspect ratio, $z_w/r_w = 1.5$, and an unconfined flame for $\sigma = 8$ at (a) 0.002, (b) 0.044, (c) 0.086, (d) 0.128, (e) 0.170 r_w/s_u^o.

length. As the flame progresses to larger values of r_f, however, the radial flame propagation speed in the cylindrical chamber becomes lower than the unconfined case because the flow is compressed in the radial direction.

Figure 5 shows the *r*-*z* plane cross-sections of the flame surface compared to that of an unconfined flame with $\sigma = 8$ and $L_u/r_w = 0$ at successive times as calculated by the flamelet model. During the early stages, corresponding to the stage labeled (a) in Fig. 5, the gas velocity is zero everywhere in the burned gas zone, and the flame shape remains the same as that of the unconfined flame. However, as the flame progresses, i.e. (b) and (c) in Figs. 5, the burned gas speed becomes negative along the *r*-axis and positive along the *z*-axis. These burned gas speeds result in a reduced propagation rate along the *r*-axis and enhanced propagation rate along the *z*-axis. The difference in propagation rates produces a distorted flame surface at stages (c), (d), and (e) – compressed in the radial direction and stretched in the axial direction, compared to the unconfined case. The acceleration of the flame front in the *z*-direction is minor for the present aspect ratio, but for higher aspect ratios, the acceleration will be more pronounced. We have reported observations of distorted flame fronts that were visualized in a cuboid-shaped chamber in our previous work [36], which provides clear experimental evidence of the deformation of the flame surface due to non-spherical confinement.

The modified evolution in cylindrical confinement is caused by the non-zero burned gas velocities imposed by the walls. Since the burned gas speed is initially zero and increases to $(\sigma-1)s_u$ when the flame reaches the wall, we define a scaled burned gas velocity as

$$\underline{\varpi} = \frac{\underline{u}_b}{(\sigma-1)s_u} \tag{17}$$

in order to generalize the flow field response to the confinement for different mixtures. Though the burned gas speeds as a function of r_f/r_w for different typical mixture compositions are very different, the scaled burned gas speeds for all the mixtures studied collapse onto a single line.

Cylindrical confinement limits the applicability of the conventional (uncorrected) constant-pressure method for flame speed calculations in two ways: 1) a disruption of spherical symmetry and 2) nonzero velocities in the burned gas zone. In the modeling results, the stretch rate was found to closely follow the spherical prediction, indicating that Eq. (15) can still be used to calculate the stretch rate using r_f and dr_f/dt from the experiments. (In fact, the stretch rate calculated using the definition of stretch as $d\ln(A_f)/dt$ and the stretch rate using (15), differ by less than 5% for $r_f < 0.6\ r_w$, resulting in negligible differences in extrapolated burning velocity and Markstein length). Therefore, for sake of simplicity in applying the correction methodology, equation (15) can be used to approximate the stretch rate without incurring appreciable errors. However, the results from the last section indicate that the zero burned gas velocity assumption commonly employed in constant-pressure flame speed calculations can be strongly violated in cylindrical chambers even when the pressure in the chamber is nearly constant. The radial propagation speed, $V_{f,r}$, can be related to the flame speed and radial burned gas speed, $u_{b,r}$, through

$$V_{r,f} = \sigma \cdot s_u + u_{b,r} \tag{18}$$

Combining Eqs. (14), (17), and (18) in the radial direction yields

$$\frac{s_{u,unc} - s_u}{s_u} = \frac{\sigma-1}{\sigma}\varpi_r \tag{19}$$

Equation (19) is a measure of the error in using the unconfined (uncorrected) relations for a given scaled burned gas speed. In Eq. (19) $s_{u,unc}$ is the stretched flame speed calculated assuming

no confinement, Eq. (14), and is, therefore, the "uncorrected" flame speed. Since the scaled burned gas speed along the r-axis, ϖ_r, has been shown to be well-approximated as a function of only r_f/r_w and is of order unity, Eq. (14) shows that the error in the unconfined assumption is proportional to $(\sigma\text{-}1)/\sigma$.

Since the confinement effect is stronger when the flame is closer to the wall, extrapolating to obtain the planar burning velocity and Markstein length using Eq. (16), assuming zero burned gas velocity over ranges of large r_f/r_w will yield erroneous results.For large stretch rates (small r_f/r_w), the calculated flame speed using (14) is consistent with flame speed data taken in a large spherical bomb [32]. Then, as the stretch rate decreases (r_f/r_w increases), the flame speed calculated using the zero burned gas velocity assumption decreases significantly due to the effect of confinement.

A flow-corrected flame speed, which accounts for the actual induced fluid motions in the confinement, can be calculated by a rearrangement of Eq. (19) using Eq. (14)

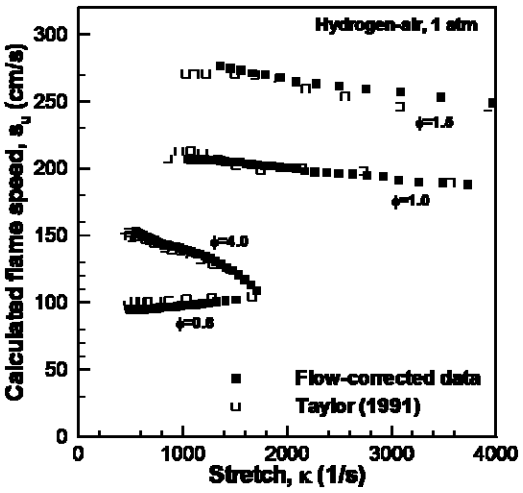

Fig. 6. Comparison of flow-corrected flame speeds obtained in a cylindrical chamber (r_w = *5 cm,* z_w/r_w = *1.5*) with flame speeds obtained from a larger bomb [32] (R_w = *30 cm*) as a function of stretch.

$$s_u = \frac{V_{f,r}/\sigma}{\left(1+\frac{\sigma-1}{\sigma}\varpi_r\right)} \tag{20}$$

Since the scaled radial burned gas speed, ϖ_r, is well-approximated as a function of r_f/r_w only (independent of mixture properties), the same correction can be used for every experiment for a given cylindrical chamber. Thus, the flow correction need only be determined once, and then the results can be used for all mixtures.

The flow-corrected flame speed, calculated using the scaled radial burned gas speed obtained from the modeling results in Eq. (20) was determined (see Fig. 6). The flow-corrected flame speed is shown to follow closely the flame speed data obtained in a larger spherical bomb by Taylor [32] – as well as other data from large bombs [41, 42] – over a much wider span of stretch rates than the uncorrected flame speed. The values of the uncorrected data are much lower than those of the flow-corrected data from the cylindrical bomb and flame speed data from large spherical bombs at large r_f/r_w. Similar results are obtained for a wide range of equivalence ratios of hydrogen, syngas, and methane mixtures which have different values for the flame speed, Markstein length, and expansion factor.

2.3 Mass burning rate measurements and kinetic analysis of $H_2/CO/CO_2/O_2$/diluent mixtures

Below, we test the performance of recent kinetic models [44-49] for flame conditions relevant to syngas applications. We present flow-corrected burning rates of $H_2/CO/O_2$/diluent flames over wide ranges of equivalence ratios, pressures, flame temperatures, and CO and CO_2

concentrations. We focus our study on low temperature conditions (<1800K) of practical interest to advanced gas turbine applications to achieve low NO_x emissions. Then, we explore the changing kinetic pathways in H_2/CO/O_2/diluent flames as pressure is increased to gain a better understanding of the fundamental kinetic phenomena in high pressure flames.

Experiments were conducted in a dual-chambered, pressure-release type high-pressure combustion apparatus (see Fig. 1). Mixtures were prepared using the partial pressure method with H_2 (99.99%), CO (99.99%), O_2 (99.5%), He (99.995%), Ar (99.997%), and CO_2 (99.99%). High purity CO stored in an aluminum cylinder was used to ensure no contamination with iron pentacarbonyl, $Fe(CO)_5$, which is readily formed in steel CO cylinders [50] and is a known flame inhibitor [51-52], as discussed in Refs. [53,5]. High-speed Schlieren photography was utilized for imaging the flame propagation and the data were processed according the flow-correction algorithm described above. The data range used for analysis was carefully adjusted for each set of conditions to minimize the effects of confinement and pressure rise, transient and nonlinear behavior, cellular instabilities and wrinkling, spiraling instabilities, and buoyancy.

2.3.1 Pressure Dependence of Mass Burning Rates of H_2 Flames

Experiments were conducted over a wide range of equivalence ratios, dilution ratios, and pressures. Mass burning rates, defined as

$$f^o = \rho_u s_u^o, \tag{21}$$

where ρ_u is the unburned gas density, are presented here since they are typically more illuminating of the global chemistry. As indicated by Egolfopoulos & Law [54], the pressure dependence of the mass burning rate is more directly related to the pressure dependence of the global reaction rate, ω, than the flame speed, which is also dependent on the change of unburned density with pressure. The pressure and temperature dependence of the global reaction rate are represented by an overall reaction order, n, and activation energy, E_a, viz.

$$\omega \sim p^n \exp\left(-E_a / R^o T\right) \tag{22}$$

Since the mass burning rate varies with the square root of the reaction rate, the pressure and temperature dependence of the mass burning rate to first order are given by

$$f \sim p^{n/2} \exp\left(-E_a / 2R^o T\right) \tag{23}$$

Of particular interest is the dependence of mass burning rate on pressure, which is represented by the overall reaction order, n, defined as [54]

$$n = 2\left\{\frac{\partial \ln(f^o)}{\partial \ln(p)}\right\}_{T_f} \tag{24}$$

for flames with mass burning rate, f^o, pressure, p, and flame temperature, T_f. Mass burning rates measured for H_2/O_2/diluent mixtures at lean and rich conditions of flame temperatures near 1600K for a variety of pressures are presented in Figs. 7 and 8. At low pressures up to about ten atmospheres, the reaction order is experimentally observed to be

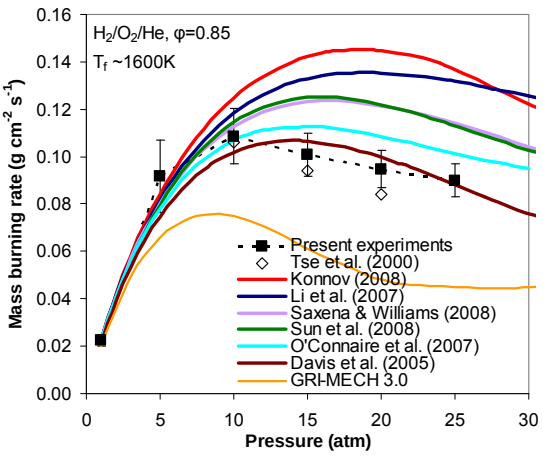

Fig.7. Mass burning rate measurements for various pressures for H_2/O_2/He flames of equivalence ratio 0.85 and flame temperature of ~1600K. Lines show predictions from the different models considered in this study [44-49].

positive, while at pressures above 10 to 15 atm, the reaction order is found to be negative. The variations of overall reaction order with pressure are qualitatively similar, but differ quantitatively for lean and rich conditions. Negative reaction orders in flames are not common but have been experimentally observed previously in N_2-diluted CH_4-air flames [54-55].

At lower pressures, predictions using recently published chemical kinetic models agree reasonably well with one another and the experimental data. However, at higher pressures, the predicted mass burning rates differ substantially from model to model and with experimental data. Much larger disparities are apparent among model predictions themselves at fuel rich conditions, with variations of nearly a factor of three in predicted burning rates. Given that the H_2 kinetic models investigated here were all validated against a wide range of (and frequently the same) data from numerous experimental apparatuses including the high pressure flame speeds of Tse et al. [25], the disparities noted amongst the predictions and with the present experimental results are noteworthy.

2.3.2 Flame Temperature Dependence of Mass Burning Rates of H_2 Flames

Mass burning rates for H_2/O_2/diluent mixtures of different flame temperatures were measured for pressures from 1 to 25 atm for equivalence ratios of 1.0 and 2.5 and flame temperatures of 1500, 1600, 1700K, and 1800K (the results are summarized, but only shown for the rich mixture in Fig. 9). The mass burning rate is higher for higher temperatures. Negative pressure dependences were observed for the 1600K case but not for higher temperatures over the pressure range studied for the stoichiometric case. Similar to the stoichiometric case, the mass burning rate is higher for higher temperatures for rich mixtures. Negative reaction orders were observed for the 1500 and 1600K cases but not for higher temperatures over the pressure range studied. The pressure of the maximum burning rate decreases with decreasing flame

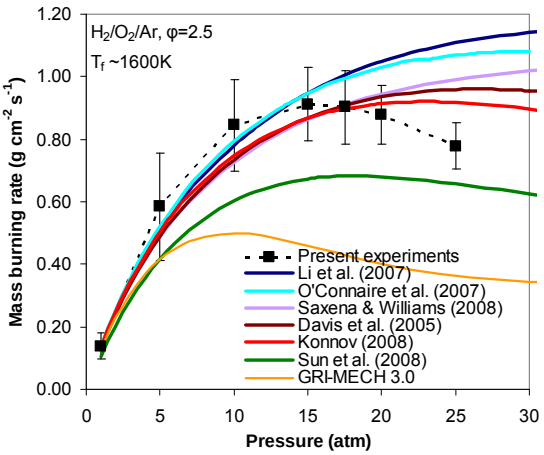

Fig. 8. Mass burning rate measurements for various pressures for H_2/O_2/Ar flames of equivalence ratio 2.5 and flame temperature of ~1600K. Lines show predictions from the different models considered in this study [44-49].

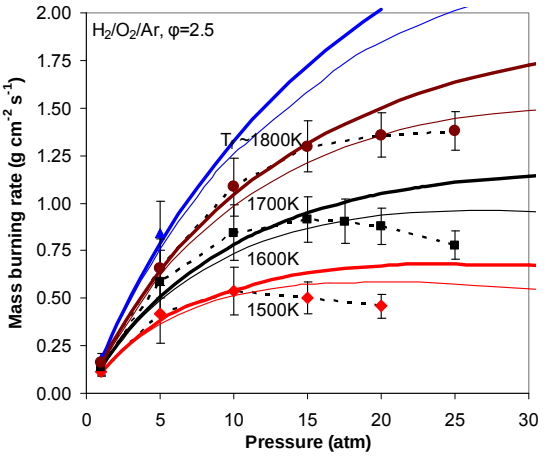

Fig. 9. Pressure dependence of mass burning rates for H_2/O_2/Ar flames of equivalence ratio 2.5 for various Ar concentrations. Symbols show experimental data, thick lines show predictions from Li et al. [44], and thin lines show predictions of Davis et al. [45].

temperature. Disagreement between the experimental data and model predictions is largest at higher pressures and lower flame temperatures. For both equivalence ratios, the temperature dependence becomes stronger with increasing pressures—indicative of a higher global activation energy, E_a, defined as [54]

$$E_a = -2R^o \left\{ \frac{\partial \ln(f^o)}{\partial (1/T_f)} \right\}_p \tag{25}$$

as pressure is increased.

The Zeldovich number, defined as [56]

$$Ze = \frac{(T_f - T_u)E_a / R^o}{T_f^2} \tag{26}$$

represents a non-dimensional activation energy corresponding in asymptotic theory to the ratio of the overall flame thickness to the reaction zone thickness. (Here, T_u is the unburned gas temperature.) Thus, an increasing Zeldovich number with increasing pressure implies a higher activation energy and smaller reactive portion of the flame. This observation of a stronger temperature dependence, and hence higher activation energy and Zeldovich number, at higher pressures is consistent with the numerical studies described below.

2.3.3 Effect of CO Addition on the Pressure Dependence of Mass Burning Rates

The pressure dependences of $H_2/CO/O_2/Ar$ mixtures of equivalence ratio 2.5 for H_2:CO ratios of 100:0, 50:50 and 10:90 are plotted in Fig. 10. The level of Ar dilution was varied for the mixtures to maintain a flame temperature of approximately 1600K. Negative pressure dependence is observed for the H_2:CO=50:50 mixture for pressures above 10 to 15 atm – slightly lower than for the pure H_2 mixture. The overall pressure dependence is quite similar for pure H_2 and H_2:CO=50:50. For H_2:CO=10:90, the data show that the mass burning rate becomes nearly independent of pressure at pressures above 10 atm. Disagreement between the experimental data and model predictions is strongest at higher pressures for all CO fuel fractions.

The mass burning rate as a function of CO fuel fraction for various pressures is shown in Fig. 11. Higher CO fractions have lower burning rates for all pressures. Additionally,

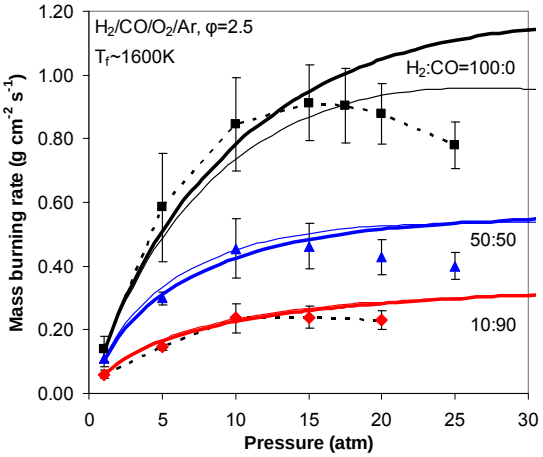

Fig. 10. Pressure dependence of mass burning rates for $H_2/CO/O_2/Ar$ flames of equivalence ratio 2.5 for various CO fuel fractions. Symbols show experimental data, thick lines show predictions from Li et al. [44], and thin lines show predictions of Davis et al. [45].

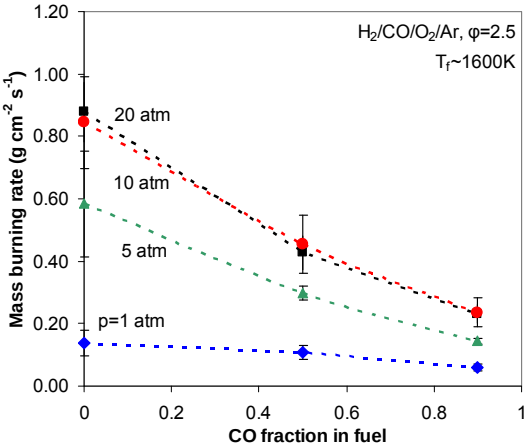

Fig. 11. Dependence of CO fraction on mass burning rates for $H_2/CO/O_2/Ar$ flames of equivalence ratio 2.5 for different pressures.

the dependence of CO fuel fraction on the mass burning rate of H_2:CO mixtures is nearly the same for all pressures. For example, the ratio of the mass burning rate of pure H_2 to that of H_2:CO=10:90 is 2.3 for 1 atm and 3.7±0.5 above 5 atm.

2.3.4 Effect of CO_2 Dilution on the Pressure and Flame Temperature Dependences of Mass Burning Rates

Mass burning rates for H_2/O_2 mixtures with CO_2 dilution were measured for different flame temperatures and pressures. Dilution with CO_2 is of interest due its high concentrations in synthetic gas mixtures and the expectation that CO_2 amplifies the pressure dependence of the mass burning rate due to its high third body efficiency relative to Ar (~5 to 1 for $H+O_2(+M)=HO_2(+M)$ (R1)).

The pressure dependences of $H_2/O_2/CO_2$ mixtures of equivalence ratio 2.5 for flame temperatures of 1500, 1600, 1700, and 1800K are plotted in Fig. 12. Negative pressure dependence is observed below 25 atm for all flame temperatures studied. Similar to Ar-diluted mixtures, as the flame temperature is increased the pressure of maximum burning rate is raised. Compared to Ar-diluted mixtures of the same flame temperature, the CO_2-diluted flames exhibit negative pressure dependence at lower pressures and even at higher temperature conditions. Strong disagreement between the model predictions and experimental measurements for mass burning rate is observed above 5 atm. Figure 13 shows the temperature dependence of CO_2-diluted flames at various pressures. Similar to Ar-diluted flames, the flame temperature dependence of the mass burning rate is stronger at higher pressures. Compared to Ar-diluted flames, however, the temperature dependence is considerably stronger – for example, $E_a = 80$ *kcal/mol* for CO_2-diluted flames at 20 atm compared to $E_a = 53$ *kcal/mol* for Ar-diluted flames at 20 atm over the temperature range from 1500 to 1700K using Eq. (25). Reasons for the stronger temperature and pressure dependence for CO_2-diluted flames compared to Ar-diluted flames are discussed in the next section.

Even though large concentrations of

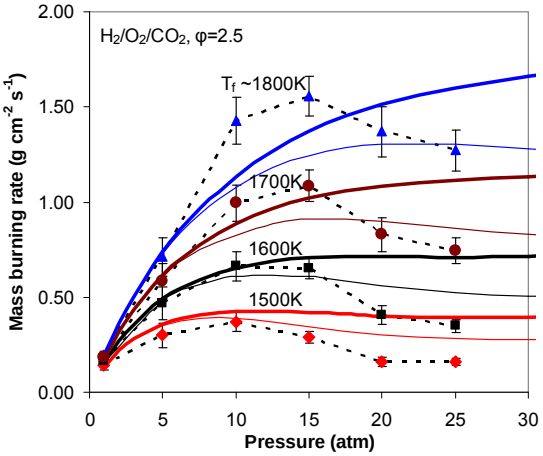

Fig. 12. Pressure dependence of mass burning rates for $H_2/O_2/CO_2$ flames of equivalence ratio 2.5 for various CO_2 concentrations. Symbols show experimental data, thick lines show predictions from Li et al. [44], and thin lines show predictions of Davis et al. [45].

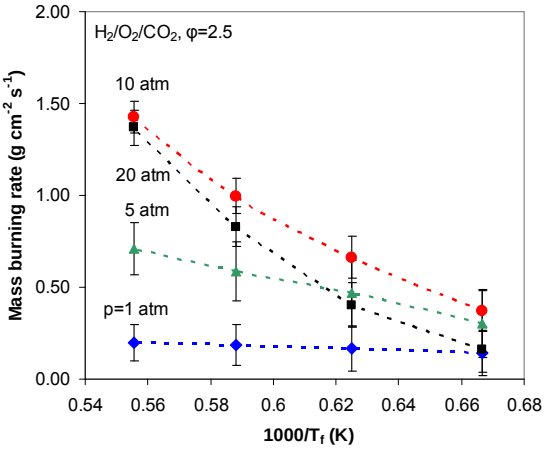

Fig. 13. Flame temperature dependence of mass burning rates for $H_2/O_2/CO_2$ flames of equivalence ratio 2.5 at different pressures.

CO_2 were present in the unburned and burned gases, the measured flame speed still demonstrated a linear relationship with stretch rate, i.e. there were no anomalous trends that would suggest significant radiation-induced burned gas motions that affect the determination of the measured flame speed as explored in our previous work [57]. Ju and co-workers showed that radiation absorption and emission are important in flames with high CO_2 dilution, since CO_2 is a strong absorber [58-59]. Chen et al. [58] indicated that spectral dependent radiation absorption must be included for any quantitative predictions of flame speed with CO_2 dilution. The effect of radiation is not considered in detail here, and we refer the reader to Refs. [58-59] for more information. The flames are approximated as adiabatic in the simulations shown in Figs. 12-13. Given that disagreement is observed between model predictions and experimental data for H_2/O_2/Ar mixtures as well as between adiabatic predictions using two different kinetic models [44-45] for $H_2/O_2/CO_2$ mixtures, the treatment of radiation in the simulations does not appear to be the sole source of disagreement between model predictions and experimental data.

Table 1. List of reactions discussed in the text.

(R1)	$H+O_2(+M) = HO_2(+M)$
(R2)	$H+OH+M=H_2O+M$
(R3)	$O+H+M=OH+M$
(R4)	$H+H+M=H_2+M$
(R5)	$H+O_2=OH+O$
(R6)	$O+H_2=OH+H$
(R7)	$OH+H_2=H_2O+H$
(R8)	$HO_2+H=H_2+O_2$
(R9)	$HO_2+H=OH+OH$
(R10)	$HO_2+OH=H_2O+O_2$
(R11)	$HO_2+HO_2=H_2O_2+O_2$
(R12)	$CO+OH=CO_2+H$
(R13)	$HCO+H=CO+H_2$
(R14)	$H+CO+M=HCO+M$
(R15)	$O+OH+M=HO_2+M$
(R16)	$H+HO_2+M=H_2O_2+M$

2.3.5 Analysis of Controlling Reactions and Kinetic Pathways

Species profiles and reaction fluxes from predictions using the mechanism of Li et al. [44] were analyzed for the lean and rich conditions of Figs. 7 and 8 at 1, 10 and 20 atm to ascertain the effect of pressure on the flame structure and kinetic pathways. Flux analyses of the radical species in the H_2/O_2 system (H, OH, O, HO_2, and H_2O_2) were conducted. The results indicate that the pressure dependent reactions that contribute substantially to the flux of H, OH, O, and HO_2 are $H+O_2(+M)=HO_2(+M)$ (R1), $H+OH+M=H_2O+M$ (R2), $O+H+M=OH+M$ (R3) for lean conditions, and $H+H+M=H_2+M$ (R4) for rich conditions (Table 1 provides a list of the reactions discussed herein). Mole fractions of H, OH, and O are lower at high pressure to such an extent for these low flame temperature conditions that the percent flux of H, OH, and O through the radical-radical recombination reactions, (R2)-(R4), is actually less at higher pressures than at lower pressures. While H_2O_2 is formed in appreciable concentrations at 20 atm, reactions that involve H_2O_2 are not responsible for significant production or consumption of any other species in the H_2/O_2 system. Consequently, H_2O_2 pathways do not appear to be important in the flames studied here (though they become important at higher pressures).

The primary cause for the pressure and temperature dependence appears to be the consumption paths of the H atom, as supported below. The main pressure-dependent recombination reaction, (R1), competes directly with the main chain branching reaction, $H+O_2=OH+O$ (R5) for H atoms. At low pressures and temperatures, (R1) is effectively radical chain terminating while (R5) participates in a chain branching loop with $O+H_2=OH+H$ (R6) and $OH+H_2=H_2O+H$ (R7), which essentially produces three H atoms for every H atom entered. If

(R1) and (R5)-(R7) are considered and (R1) is assumed to be terminating, the overall branching ratio is responsible for the well-known second limit in homogeneous kinetics

$$\frac{2k_5}{k_1[M]} = 1. \qquad (27)$$

At pressures above the third explosion limit and lower temperatures such that $2k_5/k_1[M] < 1$, H_2O_2 formation from HO_2 and its subsequent decomposition and/or reaction allows for a reaction sequence that is explosive, but the sequence is chain-carrying and thermally driven in contrast to the faster chain-branching kinetics for $2k_5/k_1[M] > 1$. Consequently, the second limit plays an important role even for pressures above the third limit in terms of characteristic reaction times. For these temperatures and pressures, HO_2 and H are present in high enough concentrations that HO_2 reacts with H through two competing channels: $H+HO_2=H_2+O_2$ (R8) and $H+HO_2=OH+OH$ (R9). Steady-state analysis of the radical pool considering (R1) and (R5)-(R9) yields a critical branching ratio,

$$\frac{k_8 + k_9}{2k_8}\frac{2k_5}{k_1[M]} = 1, \qquad (28)$$

that demarcates straight-chain from chain-branching kinetics, typically called the "extended" second limit [60-62]. The demarcation has been observed in flow reactor species profiles [60] and counterflow ignition studies [62]. The four reactions involved in the extended second limit, (R1), (R5), (R8) and (R9), also play an important role in the pressure dependence of high pressure flame kinetics, as demonstrated below.

The effect of pressure on the flame structure based on the flux of H atoms through the two pairs of competing pathways, (R1) & (R5), and (R8) & (R9), as well as H atom mole fraction is illustrated in Fig. 14. Figure 14 also shows the temperature of the extended second limit for the given pressures. The results indicate that with increasing pressure, the temperature of extended second limit increases accordingly, moving significantly toward the

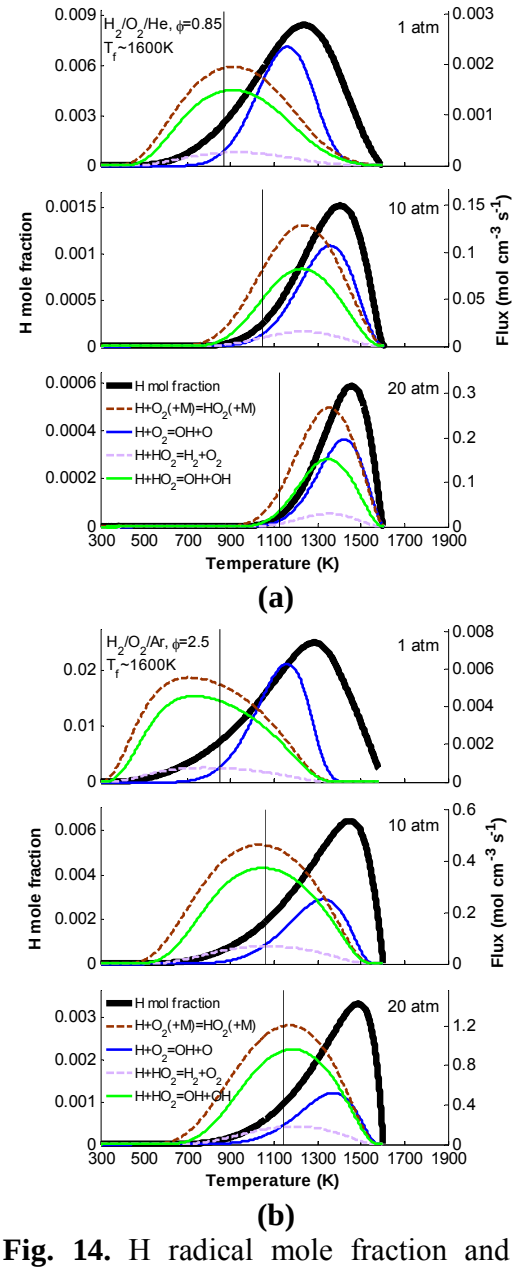

Fig. 14. H radical mole fraction and H consumption by (R1), (R5), (R8), and (R9); (a) H_2/O_2/He flames of equivalence ratio 0.85 with flame temperature of ~1600K; (b) H_2/O_2/Ar flames of equivalence ratio 2.5 with flame temperature of ~1600K. Vertical lines mark the temperature of the extended second limit for the given pressures.

post-flame region for lean and rich mixtures. Therefore, the portion of the flame that undergoes strong branching kinetics (i.e. at temperatures above the extended second limit) is reduced to a smaller temperature window at higher pressures. As pressure is increased, the flux through (R1) relative to (R5) is increased, producing more HO_2 radical instead of O atom and OH radical. The higher HO_2 concentrations lead to increased flux through (R8) and (R9) compared to (R5) as well. Overall, there is more flux through the HO_2 channels instead of strong branching channels at higher pressures. The peak H atom mole fraction is decreased substantially and also moves toward the post-flame region with increasing pressure. Furthermore, the reaction zone region in which (R1) and (R5) compete is restricted to higher temperatures and a smaller overall temperature range as pressure is increased. Similar shifts toward smaller, higher temperature windows occur in the flux profiles of other controlling reactions, including (R8) and (R9), as well as other radical and reaction flux profiles. Such a restriction of the strongly reactive portion of the flame to higher temperatures can be expressed as an increase in the overall activation energy or Zeldovich number of the mixture with pressure. The narrower, higher temperature window at higher pressures of the bulk reactivity predicted by the simulations serves to explain the stronger temperature dependence of the mass burning rate at higher pressures observed in the experiment.

Comparing Figs. 14a and 14b, the responses of the flame structure to pressure are different for different equivalence ratios. The peak fluxes of the H atom through (R1) and (R5) occur closer to the unburned region in rich flames, where the concentration of oxygen is higher. Since the peak flux of the H atom occurs at lower temperatures, where (R5) is favored relative to (R1), the peak flux through (R5) relative to (R1) is higher compared to lean conditions. At both lean and rich conditions, the mole fraction of HO_2 compared to H is substantially higher at higher pressures as a much larger portion of the flame temperature profile is below the extended second limit where (R1) is favored. Consequently, pathways involving HO_2 play a much larger role in the overall kinetics, as illustrated for rich conditions by the increased percentage of the flux through (R8) and (R9) at higher pressures in Fig. 14b.

Analyses conducted using the

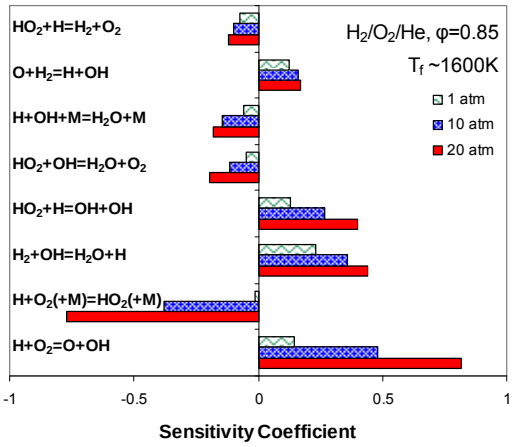

(a)

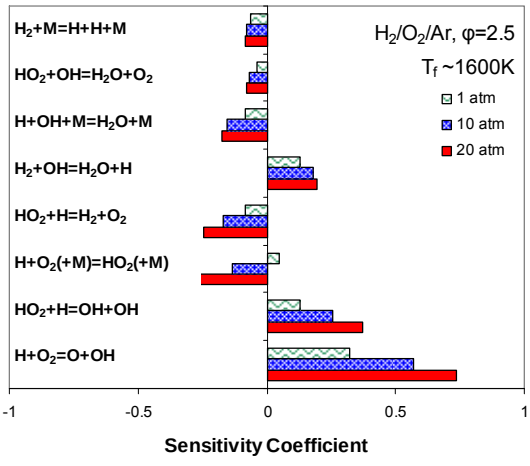

(b)

Fig. 15. Sensitivity of mass burning rate to A-factors of elementary rates; (a) H_2/O_2/He flames of equivalence ratio 0.85 with flame temperature of ~1600K; (b) H_2/O_2/Ar flames of equivalence ratio 2.5 with flame temperature of ~1600K.

mechanism of Li et al. [6] indicate that sensitivity of mass burning rate predictions, for the conditions shown in Figs. 7 and 8, to elementary rates increases considerably with pressure, as demonstrated in Fig 15. The reactions, to which the pressure dependence for rich conditions is most sensitive, are primarily reactions that involve H atoms, namely (R1), (R5), (R8), and (R9) (Fig. 15b). Rates of these four reactions define the extended second explosion limit, as discussed above. The reactions that appear to govern the pressure dependence for lean conditions are the reactions discussed above in addition to reactions involving OH radicals, namely $HO_2+OH=H_2O+O_2$ (R10) and $H_2+OH=H_2O+H$ (R7), as well as $O+H_2=H+OH$ (R6) and $H+OH+M=H_2O+M$ (R2) (Fig. 15a). Even at lean conditions, however, the rate of the branching reaction (R5) exhibits the strongest sensitivity. Reaction (R10) competes with (R8) and (R9) for HO_2 radicals and (R7) for OH radicals and inhibits the overall kinetics by converting two radicals to stable species.

In a similar manner to increasing pressure, decreasing the flame temperature through dilution restricts the reactive portion of the flame to a narrower temperature window, where branching and recombination channels are more competitive. Since recombination reactions are favored with increasing pressure and decreasing flame temperature, flux through recombination and branching channels can become roughly equal through the most reactive portion of the flame at high pressures and low flame temperatures. As a result, the sensitivity of the predictions to the rate parameters for those reactions increases dramatically. Indeed, A-factor sensitivity analyses (not shown here) of different flame temperature conditions indicate similar reaction sensitivity rankings but different magnitudes for sensitivity indices. As flame temperature is decreased, the sensitivity indices increase significantly.

Since preheated mixtures are of interest to practical IGCC systems, flame simulations were performed to discern the effect of preheat on the mass burning rate pressure dependence and prediction sensitivities to rate parameters. Two H_2/O_2/He mixtures of equivalence ratio 0.85 were studied with a preheat temperature of 700K, characteristic of isentropic compression of air from 1 to 20 atm. For one mixture, the He dilution was varied to maintain the same flame temperature of 1600K as the case in Fig. 7. For the other mixture, the He dilution was the same as the case in Fig. 7. For the case of increased dilution to maintain the same flame temperature, the pressure dependence and sensitivity results are nearly identical to the non-preheated case. For the case of fixed dilution, which results in a flame temperature of 2000K, the burning rate monotonically increases from 1 to 30 atm, and sensitivity analysis reveals the same important reactions but lower sensitivity indices. Therefore, it appears that either varying preheating or varying the dilution to alter the flame temperature have similar effects on the pressure dependence.

A-factor sensitivity analysis for the burning rate of the rich H_2:CO = 50:50 mixture of Fig. 10 at different pressures (shown in Fig. 16) reveals a nearly identical reaction sensitivity ranking, pressure dependences, and magnitudes

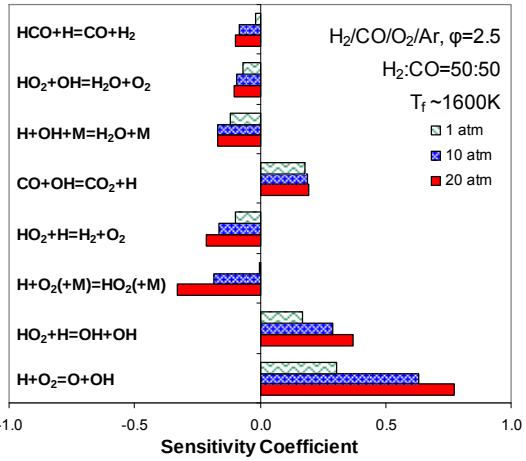

Fig. 16. Sensitivity of mass burning rate to A-factors of elementary rates for $H_2/CO/O_2/Ar$ flames (H_2:CO = 50:50) of equivalence ratio 2.5 and flame temperature of ~ 1600K.

as for a pure H_2 mixture (shown in Fig. 15). The two most notable exceptions are that $CO+OH=CO_2+H$ (R12) replaces $H_2+OH=H_2O+H$ (R7) and $HCO+H=CO+H_2$ (R13) replaces $H+H+M=H_2+M$ (R4) in the ranking. Additionally the sensitivities of those two reactions, (R12) and (R13), exhibit the same pressure dependence and approximate magnitudes as (R7) and (R4), respectively.

In terms of the effect on the radical pool, (R12) and (R7) are equivalent paths – each consume a parent fuel molecule and an OH radical and produce a stable product and an H atom. At the higher temperatures where peak reaction sensitivities and radical fluxes occur (e.g. see Fig. 14 above and Fig. 18 below), (R12) is an order of magnitude slower than (R7). Consequently, it is reasonable to expect that the burning rate will be more sensitive to (R12). Similarly, a combination of $H+CO+M=HCO+M$ (R14) and $HCO+H=CO+H_2$ (R13) produces a net path for H atom destruction that is essentially equivalent to (R4). For the pure H_2 case, (R4) consumes 7.5% of the H atoms across the entire flame. Whereas for the H_2:CO = 50:50 mixture, (R4) consumes 3.5%, (R14) 5.5%, and (R13) 3%; for the H_2:CO = 10:90 mixture, (R4) consumes 2.5%, (R14) 8.4%, and (R13) 4%. For both H_2:CO mixtures, approximately half of the HCO radicals proceed through (R14) and half through $HCO+O_2=CO+HO_2$ (R15).

If the steady state analysis for the radical pool is extended to include (R12) in addition, the equation for the extended second limit, Eq. (28), is unchanged since (R12) and (R7) both convert H atoms to OH radicals. Since the third body efficiencies of CO and H_2 are quite similar in the expressions of Li et al. for (R1), the extended second limit temperature is not predicted to change substantially. Comparison of H atom concentrations as functions of temperature for H_2:CO = 100:0, 50:50, and 10:90 reveals lower magnitudes for higher CO fuel fractions but similar profiles.

Carbon dioxide is expected to modify the flame kinetics is two main ways. First, the reverse of the reaction $CO+OH=CO_2+H$ (R12) decreases the H atom concentration and therefore serves to weaken the flame. Second, dilution with CO_2 results in an overall stronger third body efficiency of the mixture than dilution with Ar for the same flame temperature. The stronger third body efficiency of CO_2 relative to He or Ar (~5 to 1 for (R1)) substantially increases the rate of the recombination reaction (R1), which was identified as the pressure dependent reaction responsible for the most flux of radical species. Additionally, due to the high specific heat of CO_2, lower concentrations of diluent are required to achieve the same flame temperature. Therefore, there are higher reactant concentrations of H_2 and O_2 and consequently higher product concentrations of H_2O. Higher concentrations of H_2O, which has an even stronger third body efficiency of relative to He or Ar (~15 to 1 for (R1)), further increases the

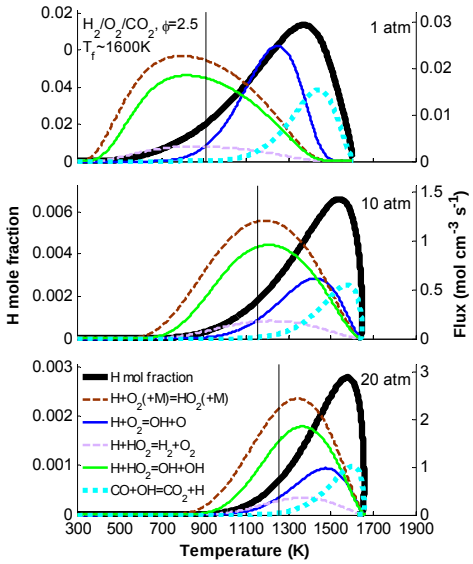

Fig. 17. H radical mole fraction and H consumption by (R1), (R5), (R8), (R9), and (R12) for $H_2/O_2/CO_2$ flames of equivalence ratio 2.5 with flame temperature of ~1600K. Vertical lines mark the temperature of the extended second limit.

rate of the recombination reaction (R1) near the post-flame region. Flux analysis reveals an increased extended second limit crossover temperature with CO_2 dilution (see Fig. 17) compared to Ar dilution (see Fig. 14b) for the same pressure, flame temperature, and equivalence ratio conditions. Compared to Ar-diluted flames of the same pressure and flame temperature, H atom concentrations and fluxes are shifted to a higher, narrower temperature region for the CO_2 diluted flames – indicative of a higher global activation energy. Additionally, there is increased flux through the recombination reaction (R1) relative to the branching reaction (R5). Since the mixture is fuel-rich, the reverse reaction of (R12) converts CO_2 to CO near the post-flame region to achieve final equilibrium concentrations. During this process, H atoms are converted to OH radicals, thus reducing the available H atom pool further. The above discussion is consistent with the trends observed in experimental data for CO_2 dilution (see Figs. 12-13) – a stronger pressure and temperature dependence of the mass burning rate as well as lower pressures of maximum burning rate compared to those of Ar-diluted flames.

Other diluents of interest to IGCC applications, N_2 and H_2O, similarly have high specific heats and high third body efficiencies relative to Ar or He. Consequently, both of these diluents are expected to strengthen the pressure dependence for a certain flame temperature – H_2O with a third body efficiency of relative to He or Ar of ~15 to 1 for (R1) to a much larger extent than N_2 with a third body efficiency of relative to He or Ar of ~2 to 1 for (R1). Simulations of H_2/O_2/diluent flames of equivalence ratio 0.85 and dilution levels chosen to yield flame temperatures near 1600K reveal pressures of maximum burning rate of 20, 10, 5, and 2 atm for He, N_2, CO_2, and H_2O respectively. Accordingly, the strength of the burning rate pressure dependence of H_2/O_2/diluent flames can be ranked by diluent as He < N_2 < CO_2 < H_2O.

The observed discrepancies between model predictions [44-49] and experiments and among model predictions themselves are noteworthy. All of the H_2 models tested here [44-45,46-48] have been validated against extensive (and frequently the same) sets of data including high-pressure burning rates [25]. Furthermore, many of the most sensitive reactions for the present conditions are highly sensitive reactions in a wide variety of combustion systems, both for H_2 and other hydrocarbons. At present, the uncertainties at these conditions can be attributed to a number of sources, including the temperature dependence of the rate constant HO_2+O/OH/HO_2/H reactions, fall-off behavior for (R1) in both pure and mixed gases, and rate constants for reactions, like O+OH+M=HO_2+M, which have typically been ignored but can affect predictions using rate constants within uncertainty limits. Analyses suggest that H atom diffusion contributes to the present uncertainties somewhat but is not the sole source of disagreement. We refer the reader to Refs. [4,6] for more detailed description of the present uncertainties, which we do not elaborate upon here.

2.4. Updated kinetic model for H_2/O_2 reaction mechanism in high-pressure flames

An updated H_2/O_2 chemical-kinetic model based on that of Li et al. [11] was formulated [63-64] to address the difficulties observed in modeling recent high-pressure flame data. Emphasis was placed on assessing the current state of knowledge of relevant elementary processes and the approach needed to achieve a rigorous solution that yields quantitative predictive capability across a wide range of conditions. The primary intent of the updated model is to incorporate a number of rate constant expressions that are more consistent with elementary reaction studies, particular for the reactions most important for high-pressure flame predictions such as H+O_2(+M)=HO_2(+M), HO_2+H/O/OH/HO_2, and H+OH+M=H_2O+M. However, substantial fundamental issues and rate constant uncertainties still remain. The updated model

reproduces the homogeneous validation targets used in Mueller et al. [61] and Li et al., flame speed validation targets used in Li et al. within ~10%, and the recent dilute high-pressure burning rate measurements of Burke et al. [4] within ~25% (compared to ~50% for Li et al.). See Fig. 18 below for the observed improvement against the flame burning rate measurements from Burke et al. [4].

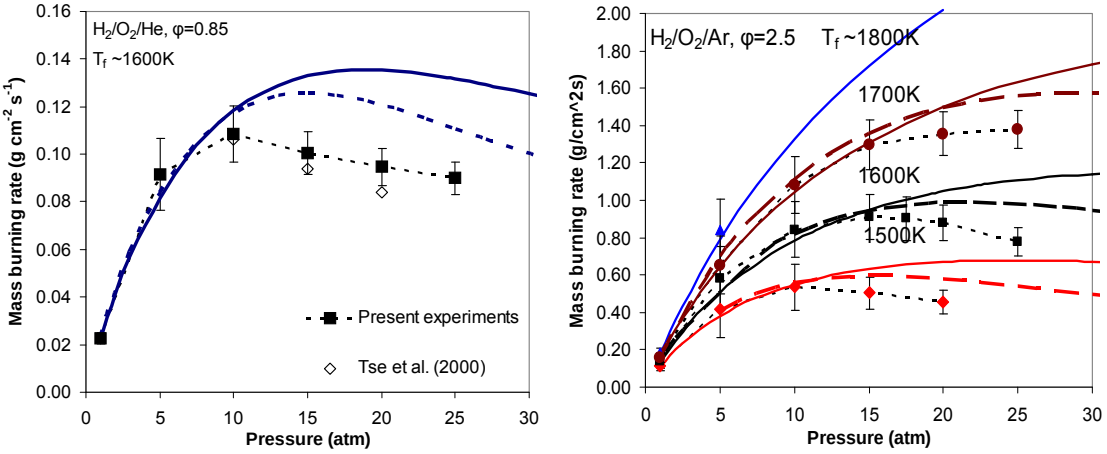

(a) **(b)**

Fig.18. Examples of model performance. Dotted lines are predictions by the present model; solid lines are predictions by the model of Li et al. [11]. (a) Laminar flame mass burning rate of H_2/O_2/He flames of equivalence ratio 0.85 and He:O_2 = 1:11.5. Symbols: experimental data [4]. (b) Laminar flame mass burning rate of H_2/O_2/Ar flames of equivalence ratio 2.5 and Ar:O_2 = 1:11.0 (T_f ~ 1500K), 1:9.52 (1600K), 1:8.2 (1700K), 1: 7.0 (1800K). Symbols: experimental data [4].

2.5. Multi-time scale method for Improved Computational Efficiency in Reacting Flow Simulations

In all combustion systems, the characteristic times of different species are very different. For example, for some kinetic systems, the minimum characteristic time of a species can be on the order of 10^{13}s whereas the maximum characteristic time of a species can be on the order of 10^{-1}s. As a result, the ignition simulation is a highly stiff problem. According to characteristic time analysis, there are only a small number of species whose order of characteristic times is 10^{-13}s.

Due to its convenience and easy controllability, the Euler method is widely used in combustion simulation. In an ODE calculation process, the time step should be defined according to the minimum characteristic time of species. Usually, 10^{-9} or 10^{-10}s is used as the time step. For mechanisms with many species, simulations require an extremely large computational time.

Although there are many methods have been developed for solving this kind of stiff ODE problems, it is still difficulty to find an efficient one to calculate the combustion process for the sharply changing of characteristic time. To address these issues, a multi time scale method is presented here and our archival paper in more detail [65].

2.5.1 The Multi Time Scale Scheme

For homogeneous ignition at constant pressure, the governing equations are

$$\frac{dY_k}{dt} = P_k(T, Y_1, Y_2, ...Y_{NS}) - D_k(T, Y_1, Y_2, ...Y_{NS}) \quad k = 1,2,...NS$$
$$\frac{dT}{dt} = f(T, Y_1, Y_2, ...Y_{NS}) \tag{29}$$

Where Y_k is the mass fraction of *k*th species, P_k and D_k are production and destruction terms, respectively, T is the temperature, NS is the total number of species.

According to the kinetic theory, the concentration of a species is included in the destruction term, so the characteristics time for destruction is given in terms of D_k as

$$\tau_k = \frac{[X_k]}{D_k} = \frac{\rho(Y_k / W_k)}{D_k} \tag{30}$$

Where τ_k is the characteristic time of the *k*th species, $[X_k]$ is the mole concentration of the *k*th species, ρ is the average density, W_k is the molecular weight of the *k*th species.

In numerical simulation, the output time step Δt_{out} is fixed according to the frequency of communication with other process, say diffusion process. At the same time, the minimum characteristic time $\tau_{\min}$ is determined by Eq. (30). The number of groups N_{mx} and the number of groups for the *k*th is determined by

$$N_{mx} = \left\lfloor Log_{10}(\frac{\Delta t_{out}}{\tau_{\min}}) \right\rfloor + 1 \tag{31}$$

$$N_k = \left\lfloor Log_{10}(\frac{\Delta t_{out}}{\tau_k}) \right\rfloor + 1 \tag{32}$$

In order to achieve convergence for each group, different time steps are adopted.

$$\Delta t_n = \frac{\Delta t_{out}}{10^n} \tag{33}$$

Where, Δt_n is the time step of the *n*th group. And according to Eq.(33), it is clear that, Δt_n is not bigger than any τ_k in the *n*th group.

2.5.2. The Point Implicit Scheme

The destruction term can be written as $D_k = Y_k \times E_k$. Therefore, we have

$$\frac{dY_k}{dt} = P_k(T, Y_1, Y_2, ...Y_{NS}) - Y_k E_k(T, Y_1, Y_2, ...Y_{k-1}, Y_{k+1}, ...Y_{NS}) \tag{34}$$

In numerical simulation:

Given states at current time $t = t^n : (T^n, Y_1^n, Y_2^n, ...Y_{NS}^n)$, states are updated during the next time step $t = t^{n+1} = t + \Delta t : (T^{n+1}, Y_1^{n+1}, Y_2^{n+1}, ...Y_{NS}^{n+1})$.

Where Δt is the time step.

$$\frac{Y_k^{n+1}-Y_k^n}{\Delta t}=P_k^n-Y_k^{n+1}E_k^n$$
$$\frac{T^{n+1}-T^n}{\Delta t}=f^n \tag{35}$$

That is:

$$Y_k^{n+1}=(Y_k^n+\Delta tP_k^n)/(1+\Delta tE_k^n)$$
$$T^{n+1}=T^n+\Delta tf^n \tag{36}$$

The superscript n in P_k^n, E_k^n, f^n means these terms are evaluated using states at time $t=t^n:(T^n,Y_1^n,Y_2^n,...Y_{NS}^n)$. For example, $P_k^n=P_k(T^n,Y_1^n,Y_2^n,...Y_{NS}^n)$.

2.5.3. Computation Procedure

Based on the equations above, the basic procedure is as follows:

a. Calculate for several steps, say 10 steps, with the round-off value of the given computer, to get the initial characteristic times of each species.

b. With the method of Eq. (31) to Eq. (33), the group number and time step for each group can be evaluated.

c. The fastest N_{PIM} groups can be calculated with point implicit method as follows:

We use states at time $t=t^n$ as the initial values ($m=1$) for iteration:

$$(T^{n,m=1},Y_1^{n,m=1},Y_2^{n,m=1},...Y_{NS}^{n,m=1})=(T^n,Y_1^n,Y_2^n,...Y_{NS}^n)$$

The iteration process are (from state $T^{n.m}$, $Y_k^{n.m}$ to $T^{n.m+1}$, $Y_k^{n.m+1}$)

$$Y_k^{n,m+1}=(Y_k^n+\Delta tP_k^{n,m})/(1+\Delta tE_k^{n,m})$$
$$T^{n,m+1}=T^n+\Delta tf^{n,m}$$

The superscript m in $P_k^{n,m}$, $E_k^{n,m}$, $f^{n,m}$ means these terms are evaluated using states from the previous iteration:

$$(T^{n,m},Y_1^{n,m},Y_2^{n,m},...Y_{NS}^{n,m})$$

For example,

$$P_k^{n,m}=P_k(T^{n,m},Y_1^{n.m},Y_2^{n.m},...Y_{NS}^{n.m})$$

Iteration ceases once

$$\sqrt{\frac{\sum_{K=1}^{NS}\left(\frac{Y_k^{n,m+1}-Y_k^{n,m}}{Y_k^{n,m}}\right)^2}{NS+1}}<RTOL_{sp} \text{ and } \left|\frac{T^{n,m+1}-T^{n,m}}{T^{n,m}}\right|<RTOL_T$$

As a result, the update states at next time step $t=t^{n+1}=t^n+\Delta t$ is

$$(T^{n+1},Y_1^{n+1},Y_2^{n+1},...Y_{NS}^{n+1})=(T^{n,m+1},Y_1^{n,m+1},Y_2^{n,m+1},...Y_{NS}^{n,m+1})$$

N_{PIM} can take on different values: if N_{PIM} is zero, it is the full multi-time scale method; and if N_{PIM} equal N_{mx}, it is the full point implicit method. Here, we take all the groups of point implicit method as one group with the maximal group time step for them.

d. For the groups other than the point implicit groups, the multi time scale method is adopted, and the main step are as follows:

After calculation of the fastest N_{PIM} groups with point implicit method, the other groups are calculated with multi time scale method from the fastest group to slowest group. For each group, according to Eq.(33), the time step Δt can be determined.

And for each species in this group,

$$Y_k^{n+1,m+1} = Y_k^{n+1,m} + \Delta t \frac{\omega_k W_k}{\rho}$$

$$T^{n+1,m+1} = T^{n+1,m} + \Delta t \left(\frac{-\sum_{i=1}^{II} h_i \omega_i W_i}{\rho c_{pb}} \right)$$

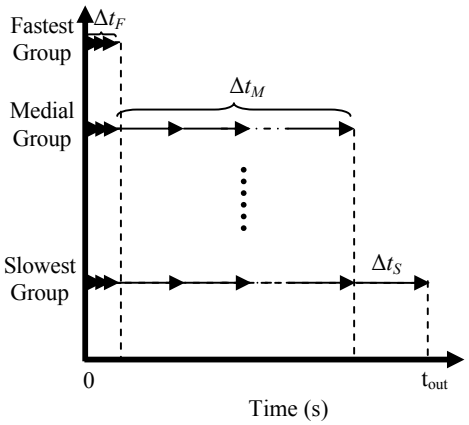

Fig.19. Multi time scale approach.

Where *II* is the number of species in this group, c_{pb} is the specific heat as constant pressure of gas mixture, h_i is the specific enthalpy of *i*th species. And only the reaction associated with the species in this group is calculated.

Iteration stops once

$$\sqrt{\frac{\sum_{K=1}^{NS}\left(\frac{Y_k^{n,m+1} - Y_k^{n,m}}{Y_k^{n,m}}\right)^2}{NS+1}} < RTOL_{sp} \quad \text{and} \quad \left|\frac{T^{n,m+1} - T^{n,m}}{T^{n,m}}\right| < RTOL_T$$

Normally, for each group calculation, few steps are needed, say 5 steps. So the other way with fixed iteration times can also be used.

The organization of the multi time scale modeling is shown as Fig. 19. First, the output time step should defined according to the interface of other parts of the whole simulation process. For the slowest species whose characteristic time is not smaller than the output time step, one calculation time is needed, and for other groups several calculation times are needed.

In the simulation process, the output time step also can be changed to satisfy the other parts of the whole model. And the maximum number of groups can be controlled easily.

2.5.4.. Studies on Homogeneous Ignition of Methane with Air

A mechanism with 53 species and 325 reaction is used. Table 2 shows the calculated ignition delay time and CPU time using MTS compared to the results with other scheme. It is seen that MTS gives the same order of accuracy among MTS and other scheme. For this case, 10^{-8} output time step is adapted, and the running time is 5.0×10^{-4}. The CPU time for VODE is roughly 10 times longer than full MTS.

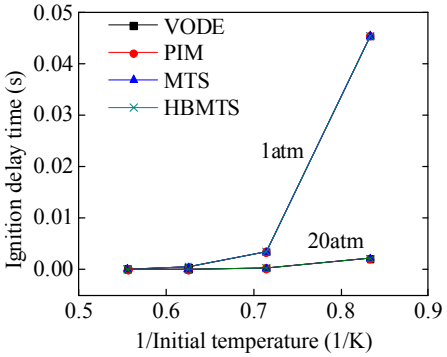

Fig.20. Ignition delay time comparison for different pressures

Table 2. Ignition delay time and CPU time comparison for different schemes with methane/air

	VODE	EULER	MTS	HBMTS	PIM
Ignition delay time (s)	3.43E-3	/	3.43E-3	3.43E-3	3.43E-3
CPU time (s)	7.94E+3	1.2E+5	6.27E+2	3.71E+2	2.43E+2

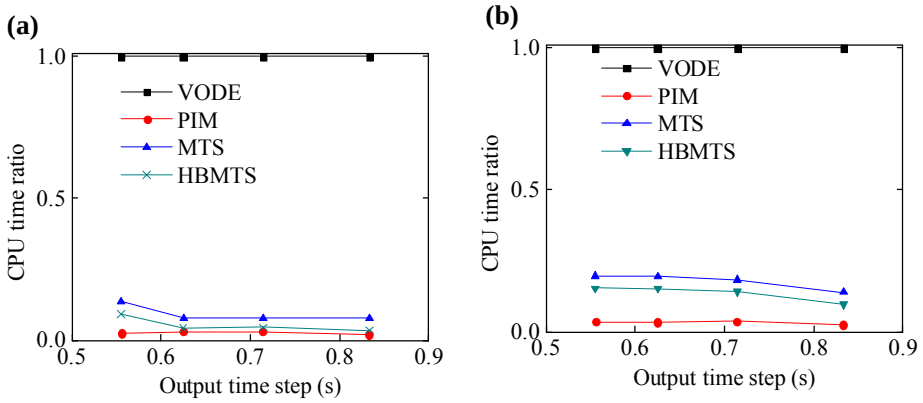

Fig.21. (a) CPU time for 1atm initial pressure, (b) CPU time for 20atm initial pressure for different output time steps

Figure 20 shows the ignition delay time comparison among these schemes. And Figure 21 shows the CPU time comparison. The results demonstrate that MTS can be used in wide range of initial pressures, and the main parameters are good agreed with other schemes.

3. Conclusions

A new fitted statistical narrow-band correlated-k (FSNB-CK) model was developed and validated for accurate radiation prediction in spherical geometry. The effects of spectral radiation absorption on the flame speed at normal and elevated pressures were experimentally and numerically investigated using the CO_2 diluted outwardly propagating CH_4-O_2-He flames. The results showed that radiation absorption with CO_2 addition increases the flame speed and extends the flammability limit. In addition, it was also shown that, unlike that conventional theory the increase of pressure augments the effect of radiation absorption. The present model not only performs better the the SNB gray gas model and the optically thin model but also showed that prediction of flame speeds for combustion mixtures with high CO_2/CO/H_2O blending requires accurate radiation modeling. Neither adiabatic nor optically thin radiation models can provide kinetic validation at high pressure and near limit conditions.

The effect of cylindrical confinement on the evolution of outwardly propagating flames and the determination of laminar flame speeds was investigated experimentally and theoretically for chambers having a length greater than their diameter. The flame appears to be relatively unaffected by confinement for $r_f < 0.3r_w$. However, for $r_f > 0.3r_w$, the boundary conditions imposed by the confinement induce non-zero burned gas velocities, resulting in a reduction of the radial flame propagation speed from the unconfined case (even for constant pressure). Extrapolation to an unstretched burning velocity using ranges of data for $r_f > 0.3r_w$ yield substantial errors using the unconfined theory, with larger errors incurred at larger r_f.

A flow correction methodology was developed to account for the non-zero burned gas velocities produced by the cylindrical chamber walls. Under the proposed scaling, the burned gas speed can be well approximated as a function of only r_f for a given chamber geometry – i.e. the correction function need only be determined once for an apparatus and then it can be used for any mixture. The proposed flow correction methodology was demonstrated to allow for flame speed and burning velocity determination for $r_f < 0.5 r_w$ with somewhat larger uncertainties. Flow-corrected burning velocities were measured for hydrogen and syngas mixtures at normal and elevated pressures.

Experimental measurements of flame speeds and burning rates, analysis of the key reactions and kinetic pathways, and modeling studies were performed for $H_2/CO/O_2$/diluent flames spanning a wide range of conditions: equivalence ratios from 0.85 to 2.5, flame temperatures from 1500 to 1800K, pressures from 1 to 25 atm, CO fuel fractions from 0 to 0.9, and dilution concentrations of He up to 0.8, Ar up to 0.6, and CO_2 up to 0.4. The experimental data show negative pressure dependence of burning rate at high pressure, low flame temperature conditions for all equivalence ratios and CO fractions as high as 0.5. Dilution with CO_2 was observed to strengthen the pressure and temperature dependence compared to Ar-diluted flames of the same flame temperature. Simulations were performed to extend the experimentally studied conditions to conditions typical of gas turbine combustion in Integrated Gasification Combined Cycle processes, including preheated mixtures and other diluents such as N_2 and H_2O.

Substantial differences are observed between literature model predictions and the experimental data as well as among model predictions themselves – up to a factor of 3 at high pressures. The present findings suggest the need for several rate constant modifications of reactions in the current hydrogen models and raise questions about the sufficiency of the set of hydrogen reactions in most recent hydrogen models to predict high pressure flame conditions relevant to controlling NO_x emissions in gas turbine combustion.

An updated H_2/O_2 chemical-kinetic model was formulated to address the difficulties observed in modeling the high-pressure flame data. The model incorporates a number of rate constant expressions that are more consistent with elementary reaction studies, particular for the reactions most important for high-pressure flame predictions such as $H+O_2(+M)=HO_2(+M)$, $HO_2+H/O/OH/HO_2$, and $H+OH+M=H_2O+M$. However, substantial fundamental issues and rate constant uncertainties still remain. The updated model reproduces a wide variety of the homogeneous validation targets flame speed validation targets with generally improved agreement against high-pressure flame targets.

Good agreement among multi-time scale (MTS) method and other schemes has been achieved in terms of concentrations of main species and temperature and ignition delay time. And the results show that MTS can be used in a wide range of initial conditions and different output time steps. The CPU time comparisons demonstrate that significant increases in computation efficiency have been gained with the use of MTS compared to some of the other solvers – reaching an order of magnitude in computational speed-up, allowing for more efficient simulations of synthetic gas combustion in gas turbine engines.

4. References

1. X. Qin, Y. Ju, Proc. Combust. Inst. 30 (2005) 233-240.
2. Z. Chen, X. Qin, B. Xu, Y. Ju, F. Liu, Proc. Comb. Inst. 31 (2007) 2693-2700.
3. M.P. Burke, Z. Chen, Y. Ju, F.L. Dryer, Combust. Flame 156 (2009) 771-779.
4. M.P. Burke, M. Chaos, F.L. Dryer, Y. Ju, Combust. Flame 157 (2010) 618-631.

5. M. Chaos, M.P. Burke, Y. Ju, F.L. Dryer, “Syngas chemical kinetics and reaction mechanisms,” Synthesis Gas Combustion: Fundamentals and Applications. Ed. T.C. Lieuwen, V. Yang, R.A. Yetter. Taylor & Francis (2009), p. 29-70.
6. M.P. Burke, F.L. Dryer, Y. Ju, Proc. Comb. Inst. (2010) accepted for oral presentation, pending decision for publication.
7. J. Qian, G. Tryggvason, C.K. Law, J. Comput. Phys. 144 (1998) 52-69.
8. B.T. Helenbrook, L. Martinelli, C.K. Law, J. Comput. Phys.148 (1999) 366-396.
9. W.S. Cleveland, J. Am. Stat. Assoc. 74 (1979) 829-836.
10. J.R. Kee, F.M. Rupley, J.A. Miller, Sandia National Laboratories Report SAND 89-8009B, Livermore, CA, 1992.
11. J. Li, A. Kazakov, Z. Zhao, M. Chaos, F.L. Dryer, J.J. Scire Jr., Int. J. Chem. Kinet. 39 (2007) 109-136.
12. L.S. Rothman, C.P. Rinsland, A. Goldman, S.T. Massie, D.P. Edwards, J.M. Flaud, A. Perrin, C. Camy-Peyret, V. Dana, J.V. Mandin, J. Schroeder, A. McCann, R.R. Gamache, R.B. Wattson, K. Yoshino, K.V. Chance, K.W. Jucks, L.R. Brown, V. Nemtchinov, P. Varanasi, *J. of Quant. Spect. Radiative Transfer* 60 (1998) 665.
13. N. Jacquinet-Husson et al., *J. of Quant. Spect. Radiative Transfer* 62 (1999) 205.
14. A. Soufiani, J. Taine, *Intl. J. Heat Mass Transfer* 40 (1997) 987.
15. W.L. Grosshandler, Radical, *Int. J. Heat Mass Transfe*r 23 (1980) 1147.
16. M.K. Denison, B.W. Webb, *J. Heat Transfer* 117 (1995) 359.
17. M.F. Modest, H. Zhang, *J. Heat Transfer* 124 (2002) 30.
18. T.K. Kim, J.A. Menart, H. S. Lee, *J. Heat Transfer* 113 (1991) 946.
19. H. Bedir, J.S. Tien, H. S. Lee, *Combust. Theory Model.* 1 (1997) 395.
20. A.A. Lacis, V.A. Oinas, *J. Geophysical Res.* 96 (1991) 9027.
21. F. Liu, G.J. Smallwood, Ö.L. Gülder, *J. of Quant. Spect. Radiative Transfer* 68 (2001) 401.
22. W.A. Fiveland, *J. Heat Transfer* 106 (1984) 699.
23. D.B. Ludwig, W. Malkmus, J. E. Reardon, J. A. L. Thomson, NASA SP3080 (1973).
24. G. Joulin, B. Deshaies, *Combust. Sci. Tech*. 47(1986) 299.
25. S.D. Tse, D.L. Zhu, C.K. Law, Proc. Combust. Inst. 28 (2000) 1793-1800.
26. G. Rozenchan, D.L. Zhu, C.K. Law, S.D. Tse, Proc. Combust. Inst. 29 (2002) 1461-1469.
27. D.R. Dowdy, D.B. Smith, S.C. Taylor, A. Williams, Proc. Combust. Inst. 23 (1990) 325-332.
28. S. Kwon, L.K. Tseng, G.M. Faeth, Combust. Flame 90 (1992) 230-246.
29. C.K. Wu, C.K. Law, Proc. Combust. Inst. 20 (1985) 1941-1949.
30. R.A. Strehlow, L.D. Savage, Combust. Flame 31 (1978) 209-211.
31. G.H. Markstein, Non-Steady Flame Propagation, Pergamon, New York, 1964, p. 22.
32. S.C. Taylor, Ph.D. thesis, University of Leeds, Leeds, U.K., 1991.
33. D. Bradley, P.H. Gaskell, X.J. Gu, Combust. Flame 104 (1996) 176-198.
34. V.F. Karpov, A.N. Lipatnikov, P. Wolanski, Combust. Flame 109 (1996) 436-448.
35. F. Parsinejad, C. Arcari, H. Metghalchi, Combust. Sci. Technol. 178 (2006) 975-1000.
36. M.P. Burke, Y. Ju, F.L. Dryer, AIAA Paper AIAA-2008-1049, 2008.
37. A.S. Huzayyin, H.A. Moneib, M.S. Shehatta, A.M.A. Attia, Fuel 87 (2007) 39-57.
38. J. de Vries, B.A. Corbin, E.L. Petersen, in: 5th US Combustion Meeting, March 25–28, 2007.
39. C. Prathap, A. Ray, M.R. Ravi, Combust. Flame 155 (2008) 145-160.
40. Z. Huang, Y. Zhang, K. Zenga, B. Liu, Q. Wang, D. Jiang, Combust. Flame 146 (2006) 302–311.

41. N. Lamoureux, N. Djebaili-Chaumeix, C.-E. Paillard, Exp. Therm. Fluid Sci.27 (2003) 385-393.
42. Z. Chen, M.P. Burke, Y. Ju, Proc. Combust. Inst. 32 (2009), doi:10.1016/j.proci.2008.05.060, in press.
43. J. Li, Z. Zhao, A. Kazakov, F.L. Dryer, Int. J. Chem. Kinet. 36 (2004) 566-575.
44. J. Li, A. Kazakov, Z. Zhao, M. Chaos, F.L. Dryer, J.J. Scire, Int. J. Chem. Kinet. 39 (2007) 109-136.
45. S.G. Davis, A. Joshi, H. Wang, F.N. Egolfopoulos, Proc. Combust. Inst. 30 (2005) 1283-1292.
46. A.A. Konnov, Combust. Flame 152 (2008) 507-528.
47. M. O'Connaire, H.J. Curran, J.M.Simmie, W.J. Pitz, C.K. Westbrook, Int. J. Chem. Kinet. 36 (2004) 603-622.
48. P. Saxena, F.A. Williams, Combust. Flame 145 (2006) 316-323.
49. G.P. Smith, D.M. Golden, M. Frenklach, N.W. Moriarty, B. Eiteneer, M. Goldenberg, C.T. Bowman, R.K. Hanson, S. Song, W.C. Gardiner Jr., V.V. Lissianski, Z. Qin, GRI-MECH 3.0. Available at: <http://www.me.berkeley.edu/gri_mech/>.
50. R.K. Tepe, D. Vassallo, T. Jacksier, R.M. Barnes, Spectrochim. Acta B 54 (1999) 1861-1868.
51. D. Reinelt, G.T. Linteris, Proc. Combust. Inst. 26 (1996) 1421-1428.
52. G.T. Linteris, M.D. Rumminger, V.I. Babushok, Prog. Energ. Combust. Sci. 34 (2008) 288-329.
53. T.C. Williams, C.R. Shaddix, Combust. Sci. Tech. 175 (2008) 1225-1230.
54. F.N Egofopoulos, C.K. Law, Combust. Flame 80 (1990) 7-16.
55. F.N Egofopoulos, PhD Thesis, Princeton University, 1990.
56. C.K. Law, Combustion Physics, Cambridge University Press, New York, 2006.
57. Z. Chen, M.P. Burke, Y. Ju, in: Society for Industrial and Applied Mathematics: 12th International Conference on Numerical Combustion, 2008.
58. Z. Chen, X. Qin, B. Xu, Y. Ju, F. Liu, Proc. Combust. Inst. 31 (2007) 2693-2700.
59. H. Guo, Y. Ju, K. Maruta, T. Niioka, F. Liu, Combust. Sci. Technol. 135 (1998) 49–64.
60. M.A. Mueller, T.J. Kim, R.A. Yetter, F.L. Dryer Fall Meeting of the Eastern States Section of the Combustion Institute, Hilton Head Island, SC, December 1996.
61. M.A. Mueller, T.J. Kim, R.A. Yetter, F.L. Dryer, Int. J. Chem. Kinet. 31 (1999) 113-125.
62. X.L. Zheng, C.K. Law, Combust. Flame 136 (2004) 168-179.
63. M.P. Burke, M. Chaos, Y. Ju, F.L. Dryer, in: Spring Technical Meeting of the Combustion Institute, Boulder, Colorado, March 2010.
64. M.P. Burke, M. Chaos, Y. Ju, F.L. Dryer, S.J. Klippenstein, Int. J. Chem. Kinet., in preparation.
65. X. Guo, W. Sun, Z. Chen, Y. Ju, Combust. Flame 157 (2010) 1111-1121.

5. Products Produced during the Research Period

Publications

1. M.P. Burke, Y. Ju, F.L. Dryer, S.J. Klippenstein, "An updated model and discussion of challenges for modeling the H_2/O_2 reaction mechanism in high pressure flames," in preparation for the *International Journal of Chemical Kinetics* in 2010.

2. M.P. Burke, F.L. Dryer, Y. Ju, "Assessment of kinetic modeling for lean $H_2/CH_4/O_2$/diluent flames at high pressures," submitted to *International Symposium on Combustion* (2010) accepted for oral presentation, decision pending for publication in the proceedings.
3. M.P. Burke, M. Chaos, F.L. Dryer, Y. Ju, "Negative Pressure Dependence of Mass Burning Rates of $H_2/CO/O_2$/Diluent Flames at Low Flame Temperatures," *Combustion and Flame* 157 (2010) 618–631.†
4. M. Chaos, M.P. Burke, Y. Ju, F.L. Dryer, "Syngas chemical kinetics and reaction mechanisms," Synthesis Gas Combustion: Fundamentals and Applications. Ed. T.C. Lieuwen, V. Yang, R.A. Yetter. Taylor & Francis (2009), p. 29-70.
5. M.P. Burke, Z. Chen, Y. Ju, F.L. Dryer, *Combustion and Flame* 156 (2009) 771-779.
6. Z. Chen, M.P. Burke, Y. Ju, "On the Accurate Determination of Laminar Flame Speed from Expanding Spherical Flames: Effect of Initial Flame Transition", *Proceedings of the Combustion Institute* 32 (2009) 1461-1469.
7. Z. Chen, M.P. Burke, Y. Ju, "Effects of compression and stretch on the determination of laminar flame speed using propagating spherical flames", *Combustion Theory and Modelling*, 13 (2009) 343-364.
8. Z. Chen, Y. Ju, "Combined effects of curvature, radiation, and stretch on the extinction of premixed tubular flames", *International Journal of Heat & Mass Transfer* 51 (2008) 6118-6125.
9. Z. Chen, X. Qin, B. Xu, Y. Ju, F. Liu, "Studies of radiation absorption on flame speed and flammability limit of CO2 diluted methane flames at elevated pressures", *Proceedings of the Combustion Institute* (2007) 31: 2693-2700.

† Feature Article on Combustion and Flame

Conference Submissions

1. Z. Chen, X. Qin, Y. Ju, "Burning properties of dimethyl ether/methane/air mixtures at normal and elevated pressures," 18th International Symposium on Transport Phenomena, Daejeon, Korea, August 2007.
2. Z. Chen, Y. Ju, "On the accurate determination of flame speeds at normal and elevated pressures by using a spherical bomb: the effect of compression and stretch (detailed chemistry)", 6th Asian-Pacific Conference on Combustion (ASPACC07), Nagoya, Japan, May 2007.
3. M.P. Burke, X. Qin, Y. Ju, F.L. Dryer, "Measurements of Hydrogen Syngas Flame Speeds at Elevated Pressures," 5th US Combustion Meeting, San Diego, California, USA, March 2007.
4. Z. Chen, Y. Ju, "The effects of flow compression on the determination of flame speeds using propagating spherical flames at normal and elevated pressures", 5th US Combustion Meeting, San Diego, California, USA March 2007.
5. Z. Chen, Y. Ju, "Combined effects of radiation, stretch and curvature on the extinction of premixed tubular flames (one-step chemistry)", 45th AIAA Aerospace Sciences Meeting and Exhibit, Reno, Nevada, USA, January 2007. No. 2006-0175.
6. Z. Chen, Y. Ju, "On the accurate determination of flame speeds at normal and elevated pressures by using a spherical bomb: the effect of compression and stretch", 45th AIAA Aerospace Sciences Meeting and Exhibit, Reno, Nevada, USA, January 2007. No. 2006-0378.
7. M.P. Burke, Y. Ju, F.L. Dryer, "Effect of Cylindrical Confinement on the Evolution of Outwardly Propagating Flames," Eastern States Meeting of the Combustion Institute, Charlottesville, Virginia, USA, October 2007.
8. Z. Chen, Y. Ju, "The stretch effect on the accurate determination of laminar flame speed using expanding flames in a spherical bomb", Eastern States Meeting of the Combustion Institute, Charlottesville, Virginia, USA, October 2007.

9. M.P. Burke, M. Chaos, Y. Ju, F.L. Dryer, "Pressure dependence of H_2 and H_2/CO Laminar Flame Speeds," International Symposium on Combustion, Montreal, Canada, August 2008.
10. Z. Chen, M.P. Burke, Y. Ju, "Studies on the critical flame radius and minimum ignition energy for spherical H_2/O_2/He/Ar flames," 47th AIAA Aerospace Sciences Meeting and Exhibit, Orlando, Florida, Jan. 2009.
11. M.P. Burke, M. Chaos, Y. Ju, F.L. Dryer, "Non-monotonic Pressure Dependence in Laminar Mass Burning Rates for Hydrogen Flames," 47th AIAA Aerospace Sciences Meeting and Exhibit, Orlando, Florida, Jan. 2009.
12. M.P. Burke, M. Chaos, Y. Ju, F.L. Dryer, "Pressure and Flame Temperature Dependence of Burning Rates of $H_2/CO/CO_2$ Flames," 6th U.S. Meeting of the Combustion Institute, Ann Arbor, Michigan, May 2009.
13. M.P. Burke, M. Chaos, F.L. Dryer, Y. Ju, "Development and validation of chemical kinetic mechanisms for synthetic gas combustion in gas turbines," 2nd International Forum on Multidisciplinary Education & Research for Energy Science, Okinawa, Japan, December 2009. †
14. M.P. Burke, F.L. Dryer, Y. Ju, "Negative pressure dependence of high pressure burning rates of H_2/O_2 flames at lean conditions," 48th AIAA Aerospace Sciences Meeting and Exhibit, Orlando, Florida, January 2010.
15. M.P. Burke, M. Chaos, Y. Ju, F.L. Dryer, "An updated model and discussion of modeling challenges in high-pressure H_2/O_2 flames," Spring Technical Meeting of the Combustion Institute, Boulder, Colorado, March 2010.
16. M.P. Burke, Y. Ju, F.L. Dryer, "Assessment of kinetic modeling for lean $H_2/CH_4/O_2$/diluent flames at high pressures," International Symposium on Combustion, Tsinghua University, Beijing, China August 2010.

†Best presentation award at 2nd International Forum on Multidisciplinary Education & Research for Energy Science, Japan